Institute for Computer Science VII
Robotics and Telematics

Bachelor's thesis

Non-invasive discrimination of lunar rock types utilizing three laser scanners at different wavelengths

Sofie Köhl

June 2023

First reviewer: Prof. Dr. Andreas Nüchter
Advisor: Jasper Zevering

Abstract

The next big step in human history is the return to the moon and to explore its subsurface. This work aims at the non-invasive identification of lunar rock types in lava tubes with simple methods and commercial sensors. Laser scanners fit requirements to explore and identify the subsurface environment and its geological structure. Using the provided intensity information possibly further characterises potential resources for future exploration and their compositional structure.

Lava tube structures are unlit cave environments that are rough and uneven. Navigating across them and bringing back potentially interesting probes is challenging.

Laser scanners on the spherical robot of the DAEDALUS project will produce 3D models of high spatial accuracy that are robust to adverse illumination conditions. These sensors also hold valuable information to identify rock types with. The recorded intensity value represents the strength of the backscattered signal and therefore provides significant information about surface properties that enable us to determine the material at hand.

We implement a method to improve the existing payload of DAEDALUS to extract intensity data and use it to identify rock types. To test our thesis this work cross-calibrates three laser scanners at different wavelengths to one range of intensities. And measures relations of intensities for each of the four rock type samples at hand. We implement a normalization rather than a full correction to true reflectance to keep a simple and fast way of calibrating the sensors. This method shows promising results for surface identification. Additionally, the detection of an ice surface on top of the stones is possible.

Zusammenfassung

Der nächste große Schritt in der Geschichte der Menschheit ist die Rückkehr zum Mond und die Erforschung seines Untergrunds. Ziel dieser Arbeit ist die nicht-invasive Identifizierung von Mondgesteinstypen in Lavatunneln mit einfachen Methoden und kommerziellen Sensoren. Laserscanner eignen sich für die Erkundung und Identifizierung der unterirdischen Umgebung und ihrer geologischen Struktur. Anhand der bereitgestellten Intensitätsinformationen könnten potenzielle Ressourcen für die künftige Erkundung und deren Zusammensetzungsstruktur weiter charakterisiert werden.

Lavartunnelstrukturen sind unbeleuchtete Höhlen, die rau und uneben sind. Es ist eine Herausforderung, durch sie zu navigieren und potenziell interessante Gesteinsproben zurückzubringen.

Die Laserscanner auf dem kugelförmigen Roboter des DAEDALUS-Projekts werden 3D-Modelle mit hoher räumlicher Genauigkeit erstellen, die auch bei ungünstigen Beleuchtungsbedingungen stabil sind. Diese Sensoren enthalten auch wertvolle Informationen zur Identifizierung von Gesteinsarten. Der aufgezeichnete Intensitätswert stellt die Stärke des rückgestreuten Signals dar und liefert daher wichtige Informationen über die Oberflächeneigenschaften, die es uns ermöglichen, das vorliegende Material zu bestimmen.

Wir implementieren eine Methode zur Verbesserung der bestehenden Nutzlast von DAEDALUS, um Intensitätsdaten zu extrahieren und sie zur Identifizierung von Gesteinsarten zu verwenden. Um unsere These zu testen, werden in dieser Arbeit drei Laserscanner mit unterschiedlichen Wellenlängen auf einen Intensitätsbereich kalibriert. Außerdem werden die Intensitätsverhältnisse für jede der vier vorliegenden Gesteinsproben gemessen. Um eine einfache und schnelle Kalibrierung der Sensoren zu ermöglichen, führen wir eine Normalisierung anstelle einer vollständigen Korrektur des tatsächlichen Reflexionsgrads durch. Diese Methode zeigt vielversprechende Ergebnisse bei der Oberflächenidentifikation. Außerdem ist die Erkennung einer Eisfläche auf den Steinen möglich

Contents

List of Figures

List of Tables

List of Algorithms

Acronyms

ALS Airborne Laser Scanner.

BRDF Bidirectional Reflectance Distribution Function.

DAEDALUS Descent And Exploration in Deep Autonomy of Lava Underground Structures.

FLANN Fast Library for Approximate Nearest Neighbors.

FoV Field of View.

HSL Hyperspectral LiDAR.

LIBS Laser Induced Breakdown Spectroscopy.

LiDAR Light Detection and Ranging.

PCL Point Cloud Library.

ROS Robot Operating System.

RViz 3D visualization tool for ROS .

SLAM Simultaneous Localization and Mapping.

TLS Terrestrial Laser Scanner.

ToF Time of Flight.

Chapter 1

Introduction

The return of humans to the moon is on the verge of realization. The planned Gateway station of NASA [1] will support the Artemis campaign [2] as a human outpost in cislunar orbit. The goal of the Artemis campaign is to revisit the Moon to explore more of the lunar surface than ever before and establish a long-term presence on the Moon. Using the Moon as a testing ground for humans venture to Mars. As a strong part of the lunar strategy of ESA, the Argonaut spacecraft [3] was approved in 2022. The lunar lander is capable of functioning as a stand-alone scientific mission or as an addition to the Artemis programme.

Returning to the Moon will be the first step towards deep space exploration. The Moon serves several purposes, scientific discovery, economic benefits, and inspiration. The return to the Moon requires new approaches to achieve exploration goals. The identification of in-situ resources such as minerals and H_2O hold high priority. To enable the production of fuel, oxygen, and construction materials on site and identify natural shelters. The compositions of rocks help us understand the volcanic activity of the Moon and potentially uncover evidence of water or other volatiles from the past of the Moon.

The Lunar Reconnaissance Orbiter (LRO) Camera found many pits on the lunar surface that might provide access to uncollapsed lava tubes. The opportunity to enter a lava tube that potentially has not changed in three billion years provides many scientific discoveries. It is a chance to see what brand-new lava flows look like. Also in an equivalent to Earth. [4] Therefore, an important scientific destiny on the Moon is its many lava tubes. Moon caves preserve the history of the Moon in a geological aspect. Rock formations are protected from the extreme weathering of the surface. Enabling us to understand its formation and evolution. The identification of mineral and rock types on the Moon holds immense importance in comprehending lunar atmospheric shifts, environmental factors, geological transformations, and potential habitability in the future. The stable temperature conditions further improve conditions for future habitation.

Different rock types may require different excavation techniques or provide varying levels of support for structural elements. This information is important to be able to efficiently plan lunar exploration and habitation efforts. It also enables us to further assess the structural integrity of lava tube formations and identify potential hazards.

We are unable to take limitless amounts of probes for further analysis out of the tubes.

We require methods that enable us to predetermine materials and their significance for further research. Return missions to Earth require significant financial resources and logistical planning. The cost of developing a spacecraft capable of returning safely from the Moon is prohibitively expensive. Additionally, lava tube environments have complex structures and we expect many unreachable regions, like high ceilings and gorges. Terrestrial Laser Scanners (TLSs) are suitable to survey rocks even in these regions. An additional identification of the rock types present in these regions helps us further understand the environment and improve systems for future exploration. A pre-assessment of rock types improves our efficiency in selecting interesting rock samples and reduces the financial resources needed to a minimum. The identification of significant probes might depend on factors such as our knowledge of the rock type or other relevant considerations.

The measured distances alone give no significant information about the material in front of the laser scanner. Most TLSs record an additional value called intensity. The intensity data that is highly associated with reflectance and sometimes used interchangeably depends on parts of the wavelength and the surface properties. This leads to the conclusion it is feasible to use intensity data for surface determination.

This work aims to use the proposed Light Detection and Ranging (LiDAR) payload of the DAEDALUS project to discriminate between lunar rock types. The main goal is to test the possibility to use LiDAR intensities for differentiating between rocks found in moon caves. Finding a method to do so without having to invasively take samples or alter the surface.

Getting an absolute reflectance or a value directly proportional to it exceeds the scope of this work. We use several laser scanners to get unique relations for each rock type, cross-calibrating the scanners with Lambertian targets called Spectralons. Using only one laser scanner with a single wavelength is unfeasible to extract spectral information [6].

This work implements a method to retrieve intensity data of three laser scanners at different wavelengths and tests it on several rock samples. These consist of four rock types found in lunar environments. We test the behaviour of our specific setup with rock samples including a thin layer of H_2O ice on top. To probe the capability of detecting the ice on top of a stone and if the implementation is able to identify the rock beneath.

In Chapter 2 we discuss the motivation of this work and the project that inspired it. Chapter 3 gives a quick overview of what else researchers investigate about laser scanner intensity and sensing rocks with it. We then continue to elaborate upon the theory and concept of this thesis in Chapter 4, explaining how LiDAR intensity works and why we use it as an indicator of surface properties. Finally, in Chapter 5 we list all hard- and software components for the test series. Elaborating upon our methods. Chapter 6 then first presents results from tests and evaluates them. We end this work with a conclusion in Chapter 7.

Chapter 2

Background

It is common for geological analysation to take a rock sample, probe it in a laboratory environment, and crush it to a powder. Taking rock probes back to Earth for further research requires significant financial resources and logistical planning. Developing a spacecraft capable of returning probes safely from the Moon is prohibitively expensive. In addition, bringing probes back from the cave environments is challenging. It requires new approaches to achieve exploration goals, like the identification of resources and history. TLSs are suitable to survey rocks even in hard to reach regions like ceilings and rocks behind gorges. This study aims for non-invasive in-situ identification of rock types in moon caves with commercial laser scanners and simple methods.

2.1 Lava tubes

For over 5 decades researchers suspected the presence of caves on extraterrestrial planets. In 2009 the LRO and the Kaguya spacecraft found lunar pits on the Moon. They potentially open into vast underground tunnels. There are several equivalents on Earth. Lava tubes arise when lava flows beneath the hardened surface, leaving a cave after it drains. The flowing lava slowly forms walls around it as the surrounding lava cools or it melts its way deeper. Researchers found about 200 pits on the lunar surface. They suspect at least 16 of these to be collapsed lava tubes with the potential for human habitation. [7, 8]

High spatial resolution cameras found potential cave entrances on several planets in our solar system. This identification is the most advanced for the Moon and Mars, including proposals for exploration methods. [9–11] The possibility of subsurface voids related to drained lava tubes opens new questions. Regarding their existence, formation process, size, and stability [12].

We expect lunar lava tubes to be significantly bigger in dimension than earth equivalents. Images from the Diviner Lunar Radiometer Experiment on the LRO leave researchers to estimate the depth of the Mare Tranquillitatis pit (one of the pits on the Moon) to be 100m. They additionally predict the temperatures in the permanently shadowed places to be stable and comfortable for human life (around 17 °C), believing the extending underground structures possibly show the same stable temperatures. [7, 8]

Another interesting lunar pit is the Marius Hills pit, the potential destiny of the DAEDALUS

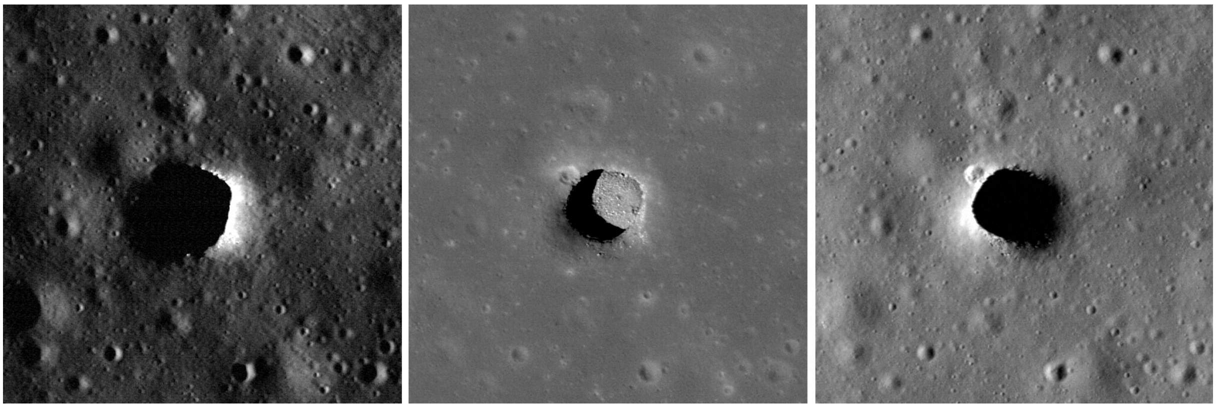

Figure 2.1: The Marius Hills pit on the Moon in different lighting. Images taken by the LRO Camera. Each image is 300m wide. The centre image gives a great view of the floor of the pit. Credit: NASA/GSFC/Arizona State University [4]

project. Figure 2.1 shows images taken by the LRO of the Marius Hills pit floor in different lighting. These images reveal the dimensions of the pit, it is about 34m deep and 65m by 90m wide [4].

Lava tubes are of particular interest due to their protected and stable environment [13]. They are protecting the inside from solar and radiation events. These stable conditions preserve a lot of the early history of a planetary body. In addition, the lava tubes and their skylights hold potential to make human habitation on extraterrestrial bodies a reality in the near future. As they possibly provide stable temperatures comfortable for humans [14]. Developing methods for initial exploring of these tubes is of high interest. The Moon is suitable to serve as a training ground for new methods and robots to get ready for Mars [15]. For which autonomy is of higher importance due to its long distance and delays to Earth.

We base this work on the DAEDALUS project [12], which we elaborate upon in the subsequent section.

2.2 DAEDALUS Project

In 2019 ESA launched a public Open Space Innovation Platform (OSIP) asking scientists for ideas to explore lunar caves. ESA chose five ideas to study in greater detail, one of them being the DAEDALUS project from the Julius-Maximilian University of Würzburg. [17–19]

DEADALUS stands for Descent And Exploration in Deep Autonomy of Lava Underground Structures, this mission design proposes a compact and tightly integrated spherical robot [12]. Figure 2.2 shows a blueprint of the robot and Figure 2.3 a 3D render. The purpose of the spherical robot is to explore and characterize the entrance and initial part of lunar lava tubes. Gathering as much information as possible from the start.

In the initial three mission phases, a crane lowers the robot into the tube, providing power supply and tethered communication. During descending, panoramic cameras and laser scanners create a 3D point cloud of the shaft, while an encoder obtains an initial depth estimate by

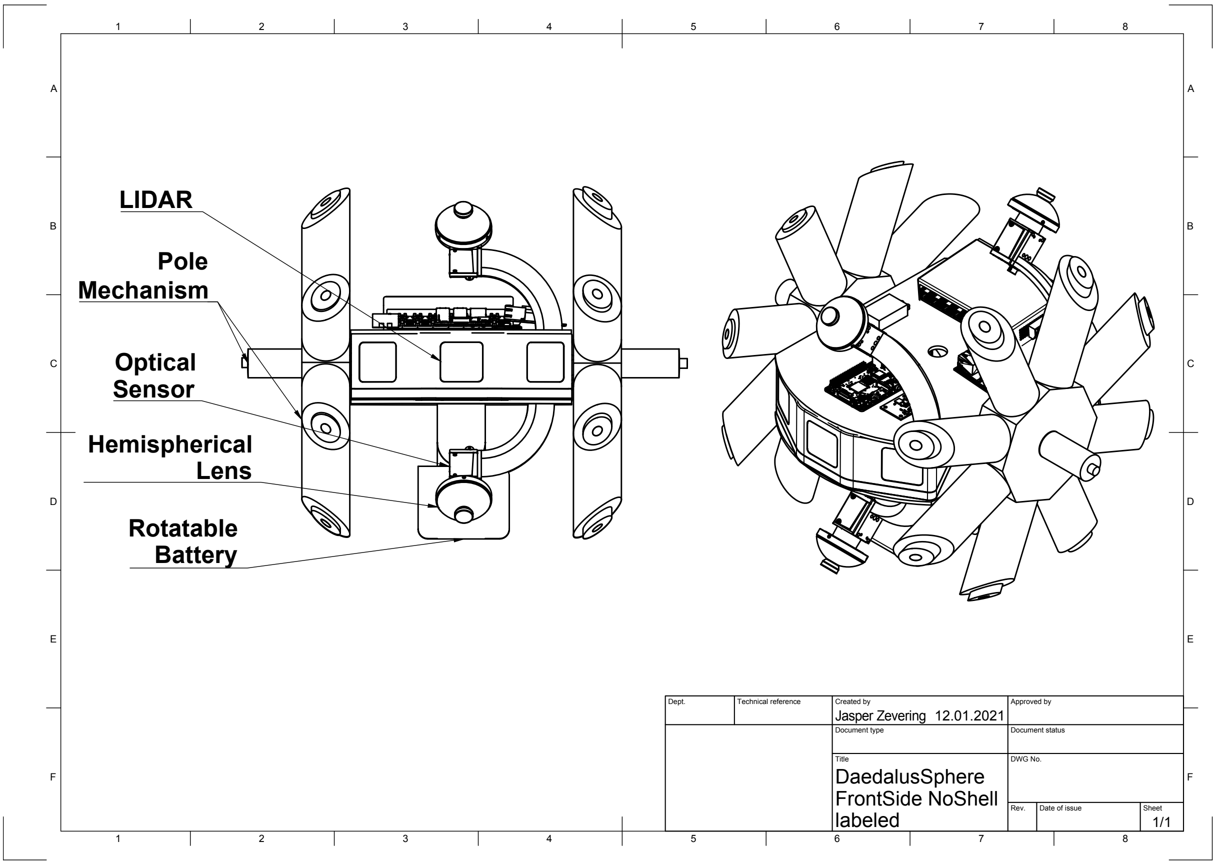

Figure 2.2: Blueprint of DAEDALUS sphere without coverage [16].

measuring the tether length. It is only in the final phase that the robot detaches from the crane and operates autonomously. In its strive for autonomy, the robot has complementary sets of optical and LiDAR sensors.

One of the goals of DAEDALUS is to characterize fresh rocks and outcrops within the lunar subsurface, as they are less impacted by space weathering.

RoboCrane [20] is another system that was chosen by ESA. Based on evaluations by the ESA, the RoboCrane is eligible to serve as one of the possible peripheral vehicles for descending the sphere.

The descent is planned in steps, stopping every 2m to rotate the sphere and scan a 360° Field of View (FoV). Resulting in an entire optical as well as LiDAR scan of the pit.

The existing LiDAR system pursues several tasks, including 3D mapping while descending, using Simultaneous Localization and Mapping (SLAM), and obtaining an initial point cloud image from an elevated point of view at the ceiling of the cave at the end of descending. This enables a structural analysis of the cave. Additionally, in combination with cameras, multi-band LiDAR systems capture a close characterization of the ground before touchdown.

For surface material characterization, the proposed design of the DAEDALUS robot includes

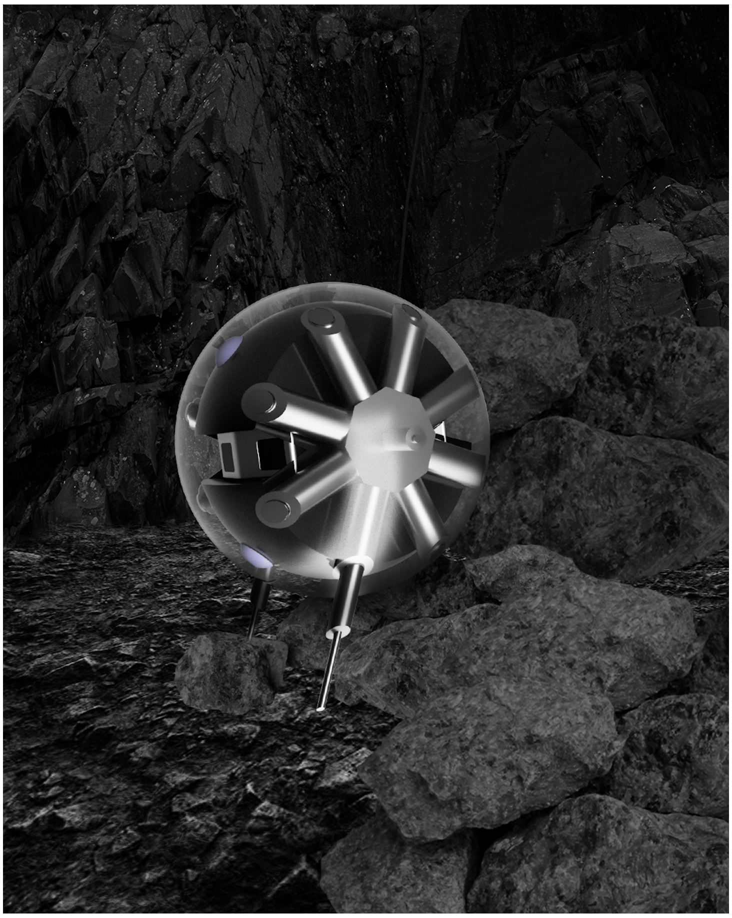

Figure 2.3: 3D render of DAEDALUS sphere in a cave environment [16].

several laser scanners operating at different wavelengths, as well as four multi spectral cameras equipped with hemispheric lenses and narrowband filters to capture imagery in four distinct spectral bands.

Using laser scanner data overcomes the adverse illumination conditions at the entrance and initial part of lava tubes and multiple wavelengths enable a spectral analysis of the environment. Single band analysis leaves little possibility for conclusions about surface material. The DAEDALUS LiDAR system will be coupled with the related measurements provided by the optical cameras. This will increase the probability of rock type discrimination and ice detection. DAEDALUS proposes at least two LiDAR wavelengths. One in the orange/red range (657nm) and one around 1500nm for ice detection.

In this thesis we use three laser scanners available to us, resulting in a total of three different wavelengths, to test the ability of the system to distinguish between rock types with the help of LiDAR intensity.

Chapter 3

Related Work

Conventionally scientists analyse and identify rock types and minerals with laboratory-intensive inventory. Either in the field, the laboratory or on a large scale on aerial imagery. In recent years the demand for non-invasive and mobile methods increased.

The concept of using reflectance as distinctive markers for various rock types is widely recognized in remote sensing [21, 22]. These methods usually do not use LiDAR intensity.

Several authors have explored the potential of utilizing TLS intensity as an indicator of rock characteristics. Some of the earliest are Pesci et al. 2008 [23], who used the intensity together with RGB data to identify lithotypes of volcanic terrains. Pesci shows that intensity data holds valuable information independent from RGB. Franceschi et al. 2009 [24] differentiated marls and limestone with an infrared laser scanner, finding that humidity highly influenced the intensity of the near-infrared sensor (1535nm). This is beneficial for our purpose to identify H_2O ice in moon caves.

Geological applications like outcrop investigations use TLS as a valuable tool to create three-dimensional models [25]. Usually, researchers drape digital photography over the point cloud data to visualize rock-type layers and discriminate between them. Using hyperspectral photography, one can differentiate between rock types. On DAEDALUS our approach has potential to be coupled with the measurements of the optical system.

Several other outcrop investigations also include LiDAR and its intensity data. For rock identification [26], as a remote sensor for rock properties [27], and to detect alteration and weathering on rock mass [28]. We expect the rock surfaces in lunar lava tubes to be significantly less affected by weathering enabling a simpler identification. Other LiDAR applications related to rocks include critical rock identification in tunnels and analysis of their stability [29], geostructural stability [30], and rock art image processing and visualisation [31]. The possibility to assess the stability of lunar lava tubes enables the identification of suitable natural shelters for human habitation.

The work of Preston Hartzell in 2014 [25] investigated the spectral possibilities of LiDAR with three laser scanners at different wavelengths, similar to this work. Their findings indicate that rock types can be successfully discriminated using calibrated TLS data fused with passive imagery. They also show that TLS intensity strength is independent of incidence angle for surfaces with roughness values typically for outcrops, these coincide with the roughness in natural rock surfaces. Their method includes radiometric calibration and passive imagery. This work focuses on normalization and does not use passive imagery, Gmöhling [32] works on the optical system of DAEDALUS. In the future process of DAEDALUS, it is possible to fuse his passive imagery with our LiDAR data.

LiDAR intensity has its limitations to discriminate between surface materials due to its lack of high spatial resolution and a large number of spectral bands. Progress in technology over the last decade allowed the development of hyper- and multispectral TLS [33, 34]. They are capable of material recognition and characterization. The LiDAR sensors rely on more than one wavelength. There are dual-wavelength systems as well as Hyperspectral LiDAR (LiDAR).

In 2013 Gaulton [35] used the intensity data of two laser scanners at different wavelengths to estimate the vegetation moisture content through ratios. Eitel did a crop foliar nitrogen assessment in 2014 [36], using green (532nm) and red (658nm) laser systems. And 2020 Chung introduced a detection method for magnesite and associated gangue minerals [37]. Other multi- and hyperspectral applications can be found in [38–41]. All these studies show that using multiple laser wavelengths holds potential to distinguish surface properties.

These applications all refer to applications on Earth. Several studies discuss lasers on Mars. For example, Sirven et al. 2007 [42] studied the feasibility of rock identification at the surface of Mars by remote Laser Induced Breakdown Spectroscopy (LIBS) and three chemometric methods. Yang conducted an open-set Martian rock classification in 2022 based on spectral signatures [43]. The Zhurong rover currently uses LIBS to detect and analyze the material composition on the Martian surface [44]. One of the objectives of the Perseverance rover that landed in the Jazero crater on Mars in 2021, is to collect samples for potential transport to Earth for analysis [45]. LIBS is an invasive method interfering with the natural planetary surface, as is taking a sample and sending it back to Earth. The goal of future research is to find methods that can identify surface properties confidently non-invasive.

Chapter 4

Approach

4.1 LiDAR concept

The following sections prescribe the working principles of laser scanners and their intensity measurements to show the feasibility of assuming LiDAR is able to identify surface materials.

Light Detection and Ranging sensors are an essential technology for the future of autonomous driving and mapping on Earth, planetary surfaces, and the like. Light Detection and Ranging (LiDAR) systems are laser scanning systems used in remote sensing. Measurements work by sending out a laser beam reflected by the environment and detected again by a sensor. Sometimes combined with optical cameras and radar sensors they help with orientation, obstacle detection, recording distances and perceiving the complex environments of the autonomous system.

Laser scanners are characterized by their functions in terrestrial and airborne applications. Terrestrial Laser Scanners (TLSs) are in use on the ground, typically static, but they are also present on mobile systems mainly for robot autonomy. Laser scanners for airborne applications (Airborne Laser Scanner (ALS)) are mounted to a flying object.

Laser scanners calculate distances to get a digital representation of the environment in 3D. There are several fundamental methods to obtain the coordinates; by the time it takes the beam to traverse from laser to target and back (Time of Flight (ToF)), by detecting a phase difference (phasing), and through the incident angle of the reflected beam (triangulation), see Figure 4.1. Triangulation is only suitable for small distances and unsuitable for the lunar cave environment. Due to the inherent unambiguousness range, phase-shift based systems are also unsuited for cave environments. Thus DAEDALUS proposes ToF sensors and in this work, we will use three commercial ToF laser scanners.

To capture the surface geometry of objects as a set of discrete sample points, referred to as point clouds, the laser beam has to be directed to multiple points in the FoV. This involves mechanical parts, typically a rotating mirror or sensor head. Conventionally point clouds consist of fields to represent points in an Euclidian space as a [x,y,z] triplet. Each point cloud point additionally has a scalar value that represents a digital number, the intensity. [12, 46, 47]

Line and Prism Scanner

Most laser scanners are multi-line scanners, they have a fixed point density for a certain distance. This results in blind spots in the point cloud and undetected targets [47–49]. In a static system, regardless of scanning time, the scanner will continuously scan points at the same positions. Figure 4.2a shows a simplified working principle for a conventional multi-line scanner. An approach to solve this problem is the prism scanner. The Risley prism uses two refractive prisms mounted in series (Figure 4.2b). Both prisms have motorized mechanisms to deflect the laser beam within a ray cone. They can both rotate independently of each other, the scanning pattern differs depending on the difference in rotation speed. The pattern can be a spiral or rosette (fig 4.2c).

4.2 LiDAR intensity

In this work, we use the additionally recorded information of the intensity from the backscattered signal to make conclusions about the material of the object in front of the sensor.

Laser scanners can use the same signal they use for range extraction to extract an intensity value [21]. Therefore, almost all conventional laser scanners provide this value in addition to spatial data. The intensity value recorded relies on the strength of the backscattered signal, which correlates to surface characteristics such as reflectance [50]. The value is generally obtained by converting and amplifying the backscattered optical power of the emitted signal [51], which is then scaled to a dynamic range.

Both used amplitude and range differ from sensor to sensor. The scanner detector is originally designed to optimize the range determination and not to measure the intensity. To make up for this, most manufacturers add modifiers that internally process the measured intensity. Since conventionally they do not provide specifications for this process, the intensity measurement is undocumented, non-standardized, and sensor-model dependent.

The spatial data of LiDAR is a significant remote sensing tool. Few studies in the past used its capability of spectral data acquisition. In recent years the efforts to exploit LiDAR intensity data and calibrate, normalize, or otherwise correct the measurements increased. Since the intensity measurements are different to conventional cameras and are too sparse, attention to them is still limited and approaches differ because of a lack of standardization and inconsistent terminology [50].

Unlike visual cameras, the measurements of laser scanners are robust to ambient illumination [52]. Which is of great advantage in unlit environments like caves. Perception technologies can be either passive or active. A visual camera passively captures images of emitted or reflected light. A LiDAR sensor actively projects pulsed laser beams, measuring the backscattered echo to map the environment. Therefore laser scans work great in adverse illumination conditions.

In almost all LiDAR applications three-dimensional object detection is an important task. The intensity measurements can be of value to detect objects without volume, like road marks in autonomous driving [53, 54].

While most laser scanner models make spatial information directly available in cartesian coordinates, intensity has to undergo processing into usable values. The intensity values typically vary strongly for a homogenous target surface, due to the influence of system-related and geometrical parameters, making them difficult to model [28]. Some of the biggest influencing environmental and geometric effects are distance, incidence angle, and atmospheric properties [5, 28, 50].

There have been efforts to correct LiDAR intensity data to use it to identify spectral signatures for a variety of applications [50, 55] in airborne laser scanning ALS [56, 57] and TLS [51, 58–60]. Either alone or in addition to other recorded spectral or spatial data. Applications vary from land-cover classification [61, 62] to tree species identification [63] to road marking detection [53, 54] to forestry [64]. Most applications using intensity adopt a normalization for it, rather than performing a complete radiometric calibration [50]. Radiometric calibration aims to provide a true reflectance value.

It is possible to model some of the effects of the parameter on the true reflectance using several distribution functions. The Oren Nayar model [65–67], the Phong model [68], and the Torrance sparrow model [69] are all Bidirectional Reflectance Distribution Functions (BRDFs), which define the spectral and spatial reflection characteristics of a surface. These models rely on the radar equation. It is possible to determine the system-specific variables of these models by scanning reference targets at various incidence angles. In a laboratory setup, the reference target gets placed at a fixed distance and scanned in steps of several degrees. Respectively scanning reference targets at various distances obtains a distance-intensity relationship for the LiDAR sensor. The collected data allows for the adoption of a mathematical function that approximates the relationships between intensity, incidence angle, and distance [70].

In this work, we want to keep the method as simple as possible. To achieve this we keep variables as stable as possible. The relationships among the variables that affect the backscattered signal then remain consistent. This includes factors such as the atmospheric conditions within the caves, intrinsic sensor variables, and the relative positions of the sensors to each other. Although variables like distance and incidence angle may change, we expect them to have a negligible impact on the relationships among the recorded values of different laser scanners, as they change by the same amount for all scanners.

Range Equation

The physical principle of laser electromagnetic waves correlates with the one of radar [66, 67]. Wagner [71] formulated an equation, assuming a beam width angle β and a circular detector of diameter D_r, to calculate the received power P_r. P_r depends on several variables, the transmitted pulse power P_t, the distance between sensor and target surface R, the target crosssection σ, and transmission factors of the system η_{sys} and atmosphere η_{atm}:

$$P_r = \frac{P_t D_r^2}{4\pi R^4 \beta_t^2} \eta_{\mathrm{sys}} \eta_{\mathrm{atm}} \sigma. \tag{4.1}$$

The target crosssection σ combines all target parameters and expresses the target characteristics as a function of target size, reflectance ρ_λ at wavelength λ and incidence angle α. Under the assumption that the laser beam footprint is smaller than the target surface and its surface is a perfectly diffuse reflector, the crosssection is described as:

$$\sigma = \pi \rho_\lambda R^4 \beta_t^2 \cos\alpha \tag{4.2}$$

When substituting Eq. 4.2 in Eq. 4.1, the radar equation simplifys to:

$$P_r = \frac{P_t D_r^2 \rho_\lambda \cos\alpha}{4R^2} \eta_{\text{sys}} \eta_{\text{atm}} \sigma. \tag{4.3}$$

The laser scanner system defines the parameters P_t, D_r, and η_{sys}, for a specific sensor they are constant. Under stable atmospheric conditions, η_{atm} is also considered constant [59]. Combining these into a constant c further simplifies Equation 4.3 to:

$$P_r \propto \rho_\lambda R^{-2} \cos\alpha. \tag{4.4}$$

The intensity value I represents a signal strength acquired through the conversion and amplification of the received power P_r. This power is transformed into a digital number that is expressed as a scaled integer value or in arbitrary units depending on the device. This means the intensity is proportional to P_r:

$$I \propto P_r \propto \rho_\lambda R^{-2} \cos\alpha. \tag{4.5}$$

In cooperation with Gmöhling [32] we aim to improve the existing payload frame of DAEDALUS by developing systems that utilize similar sensors to identify 4 common lunar rock types. The objective is to maintain the existing payload while enabling it to serve multiple purposes. M. Gmöhling focuses on an optical approach, while this work delves into utilizing multiple laser scanners. Both of these approaches align with one of the goals of DAEDALUS, which is to characterize fresh rocks and outcrops within the lunar subsurface, as they are less impacted by space weathering.

The goal is to use multiple commercial laser scanners and the spectral information the intensity holds to discriminate between four rock types. The idea for the future of the DAEDALUS project is to have four laser scanners in the spherical robot in different wavelengths. To test and evaluate the feasibility of using LiDAR intensity for rock identification in moon caves, we use three laser scanners available to us.

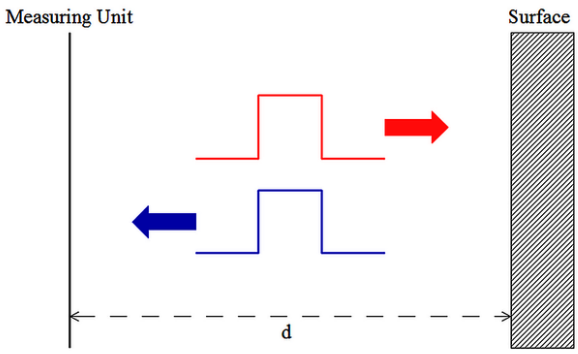

(a) ToF principle

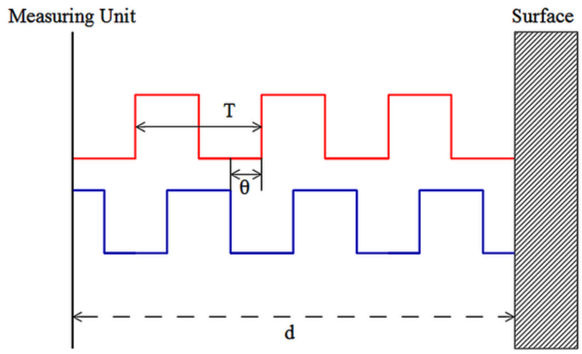

(b) Phase shifting principle

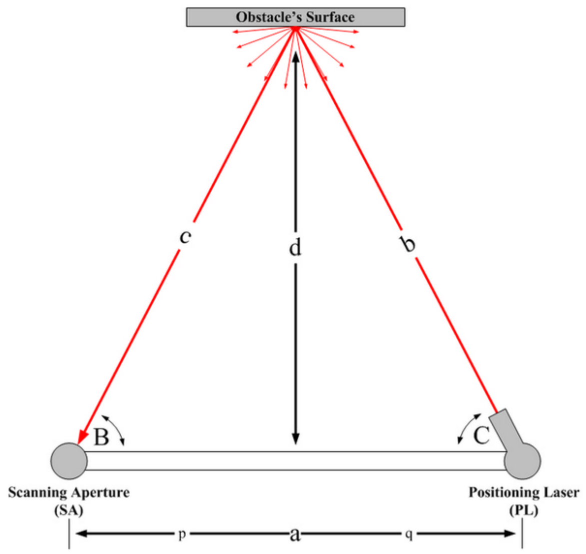

(c) Triangulation principle. PL transmits a beam and SA receives the reflected one.

Figure 4.1: Three measurement methods. The emitted pulse is depicted in red and the reflected one in blue (a and b). Distance to the target surface d; time period T (b); phase difference Θ (b). Reprinted from [47]

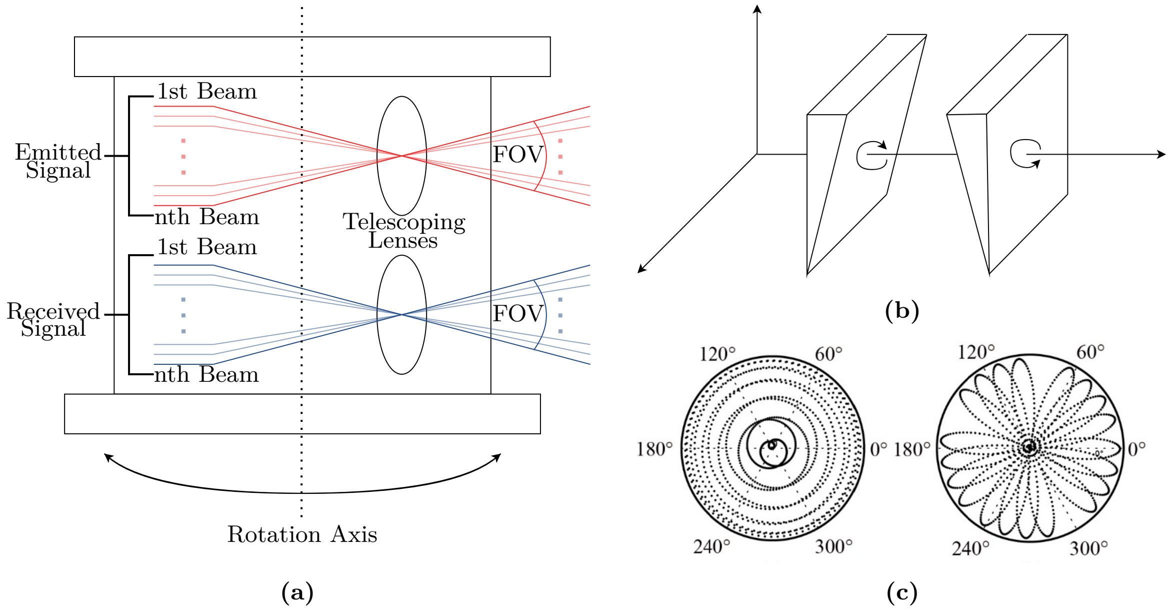

Figure 4.2: (a) is a depiction of the working principles for a n-line laser scanner adapted from [49]. Beam spacing and rotation fashion determine the resolution. The FoV angle depicted is the vertical FoV, horizontal FoV depends on how the rotation is implemented. If for example a full 360° rotation is possible, the horizontal FoV is the same. These scanners typically come in 32, 64 and 128 lines. (b) shows a simple illustration of a possible mounting position for the Risley prisms. Both prisms rotate individually around the same axis. (c) depicts a possible spiral pattern (left) and a rosette pattern (right) for a prism scanner reprinted from [49].

Chapter 5

Experimental Setup

H_2O ice shows high absorbtion in the near-infrared. For that purpose we choose one laser scanner at 1550nm. The wider the range covered, the better the distinctions made. We chose three laser scanners on the basis of availability, for that reason two of the wavelengths are rather close to each other, 865nm and 905nm. For future research we propose to swap one of these laser scanners for one in the visible orange/red range (around 657nm), this enables a better distinction between Ilmenite and thin ice layers [12]. Additionally we expect an overall increase in discrimination value when choosing more distinct wavelenghts.

We tested our approach with following tools:

- Several commercial laser scanners at different wavelengths obtaining point clouds including intensity data. Out of availability we use following three laser sensors with differing wavelenghts:
  - OUSTER os1-64 at 865nm
  - LIVOX Mid-100 at 905nm
  - RIEGL VZ-400 at 1550nm
- The Robot Operating System (ROS)
- The Point Cloud Library (PCL)
- A computer running ROS with PCL to do the calculations. The computer we use for this work runs Linux Ubuntu 20.04 with ROS noetic.
- Four spectralons as calibration targets

5.1 Technical Setup

Tab. 5.1 lists the specifications of all three devices.

[1] Range depends on the target reflectance, the higher the reflectance the higher the range

[2] variable specifications, entries represent chosen values for this work.

Sensor	OS1-64	LIVOX Mid-100	RIEGL VZ-400
Wavelength	865nm	905nm	1550nm
Laser class		Class 1 Eye-Safe	
Range (>80% reflectivity [1])	0.3 m-120 m	1 m-260 m	1.5 m-280 m
Range Accuracy 1σ	$\pm 3cm$	$\pm 2cm$	$\pm 0\,5cm$
Output rate points/sec	2,621,440	300,000	up to 122,000
Vertical FOV	45°	38.4°	10°[2]
Horizontal FOV	360°	98.4°	6°[2]
Vertical resolution	64 channels	increasing over time	0.01°[2]
Horizontal resolution	1024	increasing over time Â´	0.01°[2]
Weight	≈495g	≈2200g	≈9600g
Power consumption	14W-20W	30W (average)	65W (average)
Temperature range	−40 °C∼50 °C	−20 °C∼65 °C	−10 °C∼50 °C

Table 5.1: Specifications for OUSTER, LIVOX and RIEGL laser scanner.

5.1.1 OUSTER os1-64

The OUSTER os1-64 laser scanner is a conventional 64-line laser scanner, causing a limitation in resolution [72–74]. For the tests done in this work, the OUSTER is not ideal. The sample sizes are around 5cm (except for one Basalt sample B3) which results in <20 unique points measured on them by the OUSTER sensor. Refer to Figure 5.7a and 5.7b for a visual representation.

For calculation of the mean intensity we use more values ($<10^3$), due to the fact that the OUSTER rescans the same points. These values are from point repeats and not unique points. The limited unique points cause a transformation to fail due to insufficient precision. We are unable to consistently select manual points for all 3 point clouds that correlate to approximately the same point, which is necessary for calculating a transformation from one laser scanner system to another. Additionally, if the transformed point for the OUSTER system does not exist exactly, searching for the surrounding neighbours does not work with PCL. Therefore we opt for manual centre point selection.

Connection to Laptop

We connect the OUSTER sensor to a laptop through an ethernet cable that feeds into an ethernet hub connected to the computer. The ethernet cable feeds into an interface box connecting directly to the sensor. A power supply adapter connects the interface box to power. Ouster Inc. provides consumers with multiple drivers for their sensors. We install the provided ROS driver (`https://github.com/ouster-lidar/ouster-ros`). The main node of the driver takes the sensor data and publishes it as standard ROS topics. We use the published sensor_msgs/PointCloud2 message.

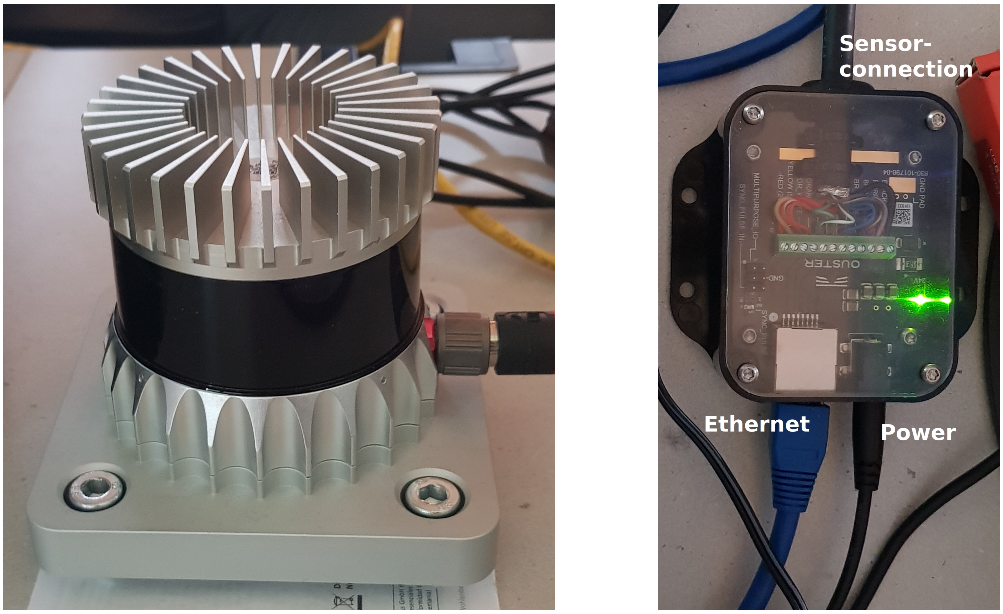

(a) **(b)**

Figure 5.1: Photography of the OUSTER os1-64 (a) and its interface box (2).

5.1.2 Livox

The LIVOX Mid-100 is a high-performance LiDAR sensor, used for multiple applications [49]. It consists of three LIVOX Mid-40s to increase its FoV [48]. Each of the Mid-40s operates at a wavelength of 905nm. The Mid-40s use Risley prisms (4.1) to record non-repetitive points in a rosette pattern becoming denser over time (Fig. 5.3). The centre of the flower shape has the highest point density from the beginning, observable in Figure 5.3.

The sensor we use in this work sits in an acrylic globe (Fig. 5.2) with a power supply by a lithium polymere Battery. The Julius-Maximilians University of Würzburg tested the Mid-100 for DAEDALUS and placed it in this prototype.

Connection to Laptop

We connect the LIVOX Mid-100 to the LIVOX converter which connects via ethernet to the same hub that feeds into the laptop. Livox Tech too provides a ROS driver (`https://github.com/Livox-SDK/livox_ros_driver`) for their device. The driver starts the laser scanner and publishes its point cloud as a sensor_msgs/PointCloud2.

5.1.3 Riegl

The RIEGL VZ-400 is a configurable line scanner. Depending on the application one can define line resolution and FoV for the device. The entire sensor head can rotate, making the horizontal FoV 360° maximum. While the vertical FoV is 100°, ranging from $-40°$ to 60°. We choose the RIEGL FoV as small as possible to still have the whole rock sample in view but no unneeded

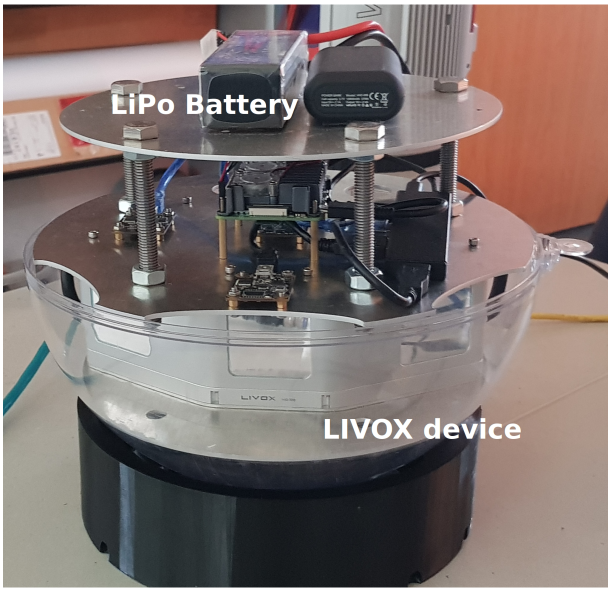

Figure 5.2: LIVOX Mid-100 in acryl Globe. The LIVOX converter is located beneath the device. We dont use the computer in between the device and battery of the prototype in this work.

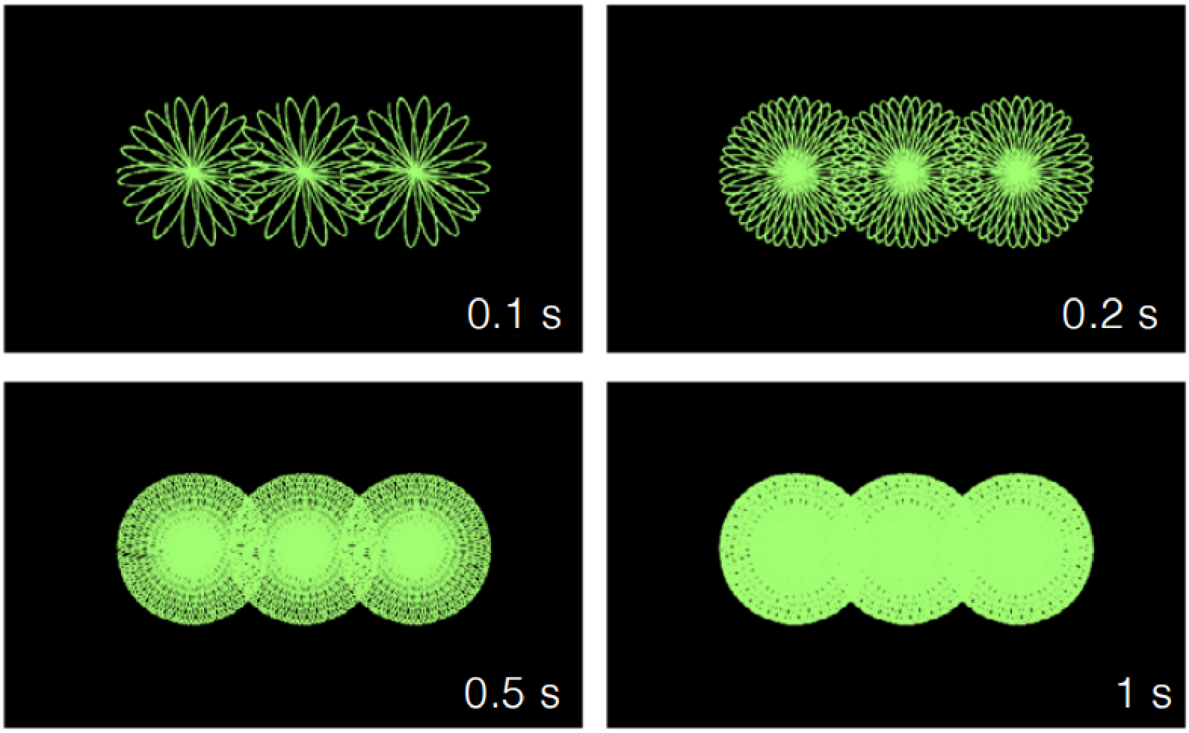

Figure 5.3: LIVOX Mid-100 point cloud pattern. The point cloud consists of 3 rosette shapes. Each of the Mid-40s inside the MId-100 produces one rosette. The density changes over time. Reprinted from [48]

Figure 5.4: Frontal View of the RIEGL VZ-400

background points and ensure fast speed (estimated 46s per scan). We list specifications in Tab. 5.1.

Connection to Laptop

The RIEGL device has a battery, but out of convenience we connect the sensor to a power outlet via a power cable. The device sends its data through an ethernet cable to the hub, which connects to the laptop.

The resulting point cloud message consists of a sensor_msgs/PointCloud. Note that this is another type of message than the other laser scanners provide. All point cloud messages get converted to the same type in processing.

Intensity Value

RIEGL provides more detailed information about their laser scanner VZ-400 [75]. Conventionally laser scanners provide the intensity measurement as amplitude reading without specifying any physical meaning. RIEGL Laser Measurement Systems (RIEGL LMS) calibrates all their devices at their facilities [76]. The RIEGL VZ-400 provides a calibrated amplitude reading (intensity). The VZ-400 provides every amplitude reading A_{dB} in decibels (dB). It describes the ratio between the measured optical amplitude of the reflected beam P_r against the detection

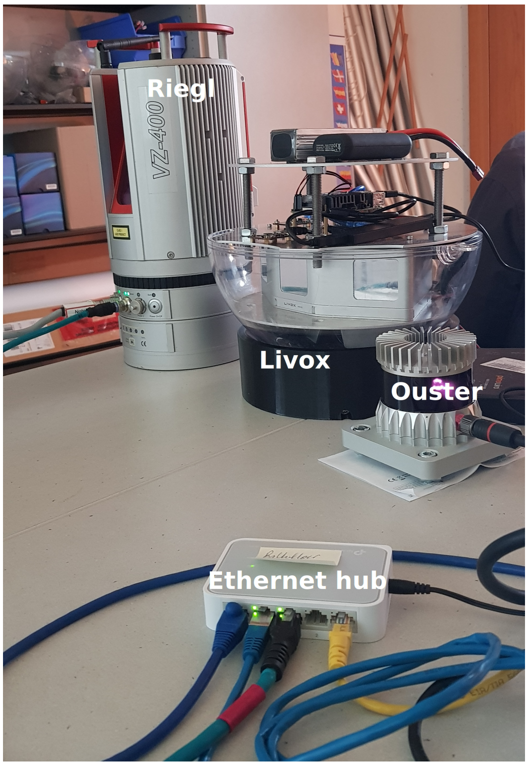

Figure 5.5: All scanners in the setup we work with. From left to right the RIEGL, LIVOX, and OUSTER sensor sit fixed in a row. The LIVOX is situated inside a DAEDALUS prototype. All laser scanners connect to an ethernet hub (at the bottom of image).

threshold P_{textDL}:

$$A_{\mathrm{dB}} = 10 \cdot \log \frac{P_r}{P_{\mathrm{DL}}}. \tag{5.1}$$

P_{DL} is the minimum detectable input power. To calibrate the amplitude, the VZ-400 varies the P_r over its dynamic range using different calibration targets and storing the internal and uncalibrated amplitude [76].

5.2 Robot Operating System ROS

The Robot Operating System (ROS) (`http://wiki.ros.org`) is an open-source meta-operating system for robot operations providing libraries and tools [77, 78]. It provides services like hardware abstraction, communication between processes, package management and many more. ROS runs on Unix-based platforms such as Ubuntu and Mac OS X on which it is primarily tested.

For this work we use packages, message types, and service types. Packages organize ROS software. Besides others, it might contain nodes, ROS-dependent libraries, and datasets.

The computation graph is a peer-to-peer network of nodes [77, 78]. The following concepts provide data to the Graph in several ways:

Nodes
Nodes are the runtime processes that perform computations in ROS. Typically many nodes make up the robot control system. As an example: one node might address a laser scanner to start a scan, one receives data from the sensors and interprets the data to point clouds, and one receives these point clouds for computations. In the case of this work, we use nodes to communicate directly with the laser scanners without a robot system included.

Master
The Master provides name registration and lookup.

Parameter Server
A parameter server stores parameters at a central location multiple nodes can access.

Messages
Nodes pass data structures called messages among themselves. For this work, most messages include point clouds. Either as a message defined by the sensor_msgs (further reference: `http://wiki.ros.org/sensor_msgs`) package or PCL (5.3). For this work its sufficient to assume the point cloud message is an unstructured list of points. With each point having information on euclidian coordinates and intensity at this point.

Topics
Messages get published and subscribed via topics.

Services

Bags
Bags can store messages and replay them.

Figure 5.6 shows the structure of nodes and messages.

5.3 Point Cloud Library PCL

PCL (see `http://pointclouds.org`) is an open-source library under a BSD license for n-dimensional point clouds and 3D geometry processing [79, 80]. It is fully integrated with ROS. The library provides most mathematical operations based on the open-source template library Eigen. While Fast Library for Approximate Nearest Neighbors (FLANN) provides the base for the k-nearest neighbour search operations.

PCL contains a collection of 3D proccessing algorithms for point clouds. Including, but not limited to, filtering, feature estimation, surface reconstruction, model fitting, segmentation, and registration. PCL aims at keeping the implementation clean and compact. To achieve this goal, for each algorithm a base class is defined. To use an algorithm, you create an object of it, set the input point cloud and relevant parameters, and finally invoke the compute (or filter, segment, etc.) function.

The PCL features we use in this work mainly consist of their point cloud classes and k-d-tree search, to simplify working with the sensor data.

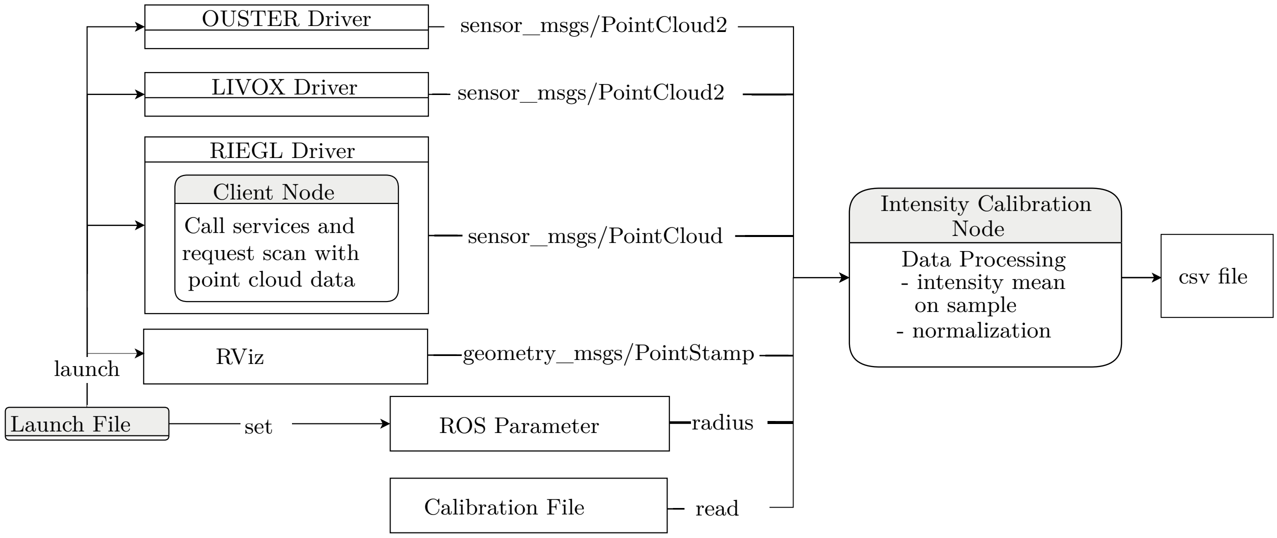

Figure 5.6: ROS node structure of analysis. A launch file sets parameters and launches the laser scanner (OUSTER, LIVOX, and RIEGL) drivers. These start scans an send out messages cointaining the point cloud data. The process (node) calculating the mean intensities writes all results into a CSV file.

5.4 Point density

The densities for all point clouds differ significantly. As long as the RIEGL device is scanning the set FoV, the ROS node is storing new point cloud messages from the other two devices. After the approximately 46s (estimated as scan time by the RIEGL device), the RIEGL sends out its point cloud, and the process stops storing new messages. Instead all point clouds are converted to a PCL point cloud type for further processing. Figure 5.7 depicts all point clouds in comparison for the Dunite sample D2.

Because the OUSTER os1-64 is a conventional line scanner its point cloud density does not change over time. Therefore, the point cloud has the lowest density of all three point clouds at the end of the scan time. After removing outliers the sample surface point quantity lies below 10^3. In Addition these points are not unique, they are rescans of the same few positions on the sample. Point density of unique points are < 20.

The RIEGLs density is significantly higher despite it also being a line scanner. The number of points after removing outliers also lies below 10^3, but these points are unique. We chose a vertical and horizontal resolution of 0.01° (Tab. 5.1). To keep a scanning time under 1min we opt for this resolution, which brings sufficient coverage of the sample surface.

The LIVOX Mid-100 achieves the highest density on the sample surfaces with quantities in 10^4. Due to the fact of its density becoming higher over time and because we place the sample inside the centre of the rosette, which has the highest density on the point cloud.

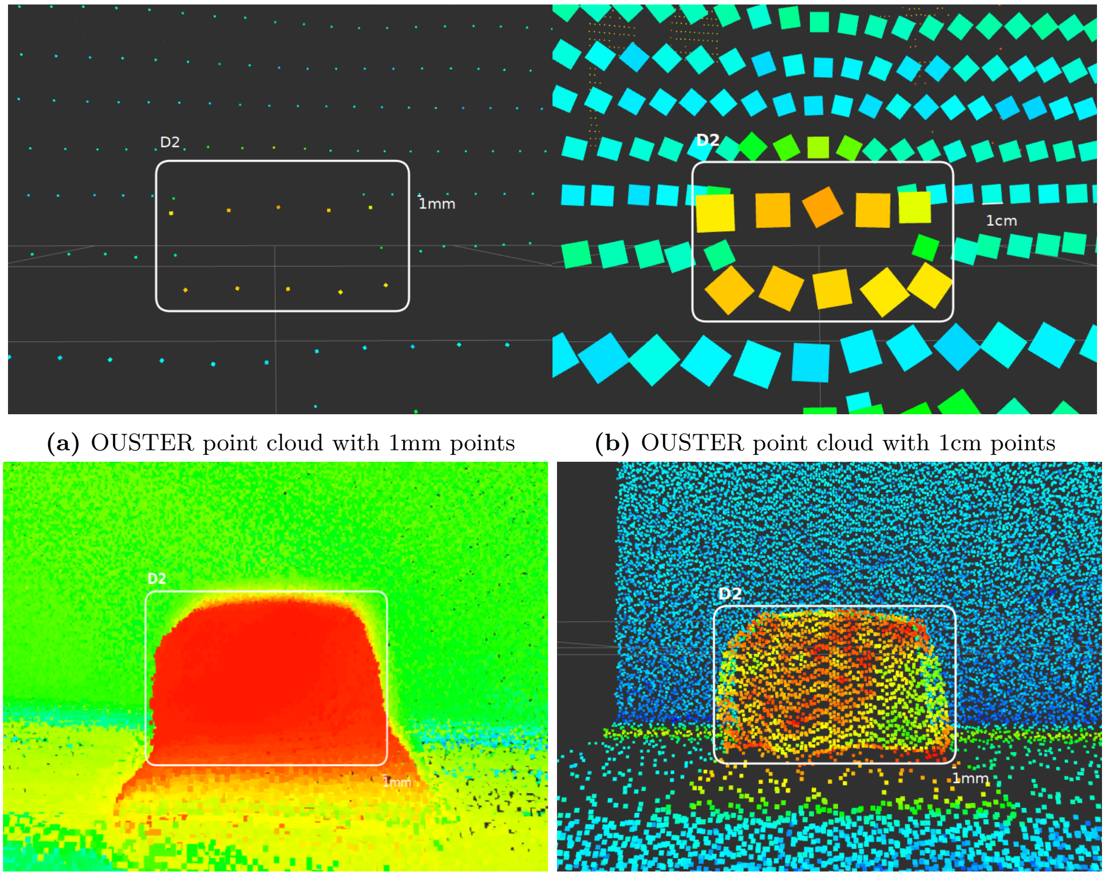

(a) OUSTER point cloud with 1mm points **(b)** OUSTER point cloud with 1cm points

(c) LIVOX point cloud with 1mm points **(d)** RIEGL point cloud with 1mm points

Figure 5.7: Received point clouds for dunite (D2) rock sample. Visualized with RViz. (b) shows the point cloud from the OUSTER sensor with 1cm big points to have a better visual of the intensity differences (color) of the sample and background. The point clouds (a), (c), and (d) all have points sized 1mm for better point density comparison.

5.5 Data Processing

We provide our code in `https://gitlab2.informatik.uni-wuerzburg.de/s391055/rock_analysis`. This excludes three files written for the RIEGL ROS driver. This code is listed in Appendix B. The following steps are necessary to scan the samples and receive the normalized mean intensities:

- Manually specifying the centre points for the sample in the point clouds
- Connecting all laser scanners to a power source and the computer that runs the ROS processes.
- Setting a sample in front of the laser scanners
- Launching the scans

After we start all laser scanner drivers, they start the scanners and publish one point cloud topic each. While the driver for the RIEGL device only publishes the entire point cloud after the whole scan finishes. The OUSTER scanner sends new messages each time the points are newly scanned and the LIVOX scanner constantly publishes messages containing new unique points while scanning. After the RIEGL scanner finishes its scan the process stops collecting point cloud messages and converts all point clouds to a PCL point cloud type for further processing.

Without going into greater detail we assume all point clouds as unstructured lists of 3D points [21]. This means we can not use prior information because the list does not follow any specific order. Every point in the list is a triplet of scalars $p_i = [x_i, y_i, z_i]$. Additionally the point cloud safes the intensity value I for each point. A common problem in point cloud processing is finding all points inside the cloud that are inside a given sphere with radius r and centred in a keypoint $k = [x_k, y_k, z_k]$ [21]. Alias the problem is to find all points which satisfy:

$$||p_i - k|| < r. \tag{5.2}$$

This approach is impractical for big datasets. To solve it one needs to calculate the distance to the center for each point in the point cloud. For large data sets, as point clouds typically are, this takes a lot of computation time. We cannot limit the data set because we do not have prior information about the contained points.

Computating the neighbours of one point in the point cloud is a common query on point clouds. Therefore, multiple solutions to perform this computation efficiently exist. The Point Cloud Library provides a class to perform a k-nearest neighbour search with a set radius. It uses a k-d-tree search to efficiently select all points within the sphere. We use this algorithm to sort out points in the point clouds to get a reduced data set of points preferably from the sample surface. By manually selecting the centre on the sample surface and specifying a radius for the nearest neighbour search.

We select a centre point in each point cloud system manually. Improvement in the future is necessary for greater autonomy.

After converting all point clouds and getting a reduced dataset of points around the manually selected centre, the data set undergoes further reduction. To limit outliers we perform a distance check on all neighbours, by removing all points that are further away or closer to the laser scanner than the centre point by a certain threshold t. Let d_k be the distance of the laser scanner to the manually selected centerpoint and d_i the distance of the point p_i to the laser scanner, then we find all points that satisfy

$$||d_k - d_i|| < t. \tag{5.3}$$

This removes points that are possibly in the fore- or background and not on the surface plane we want to identify.

At last the application of a 95% sigma band limits outliers of intensity values. The mean intensity I_m is calculated as arithmetic mean. Let n be the number of points on the sample surface and I_i the intensity at p_i, then:

$$I_m = \frac{\sum_{i=1}^{n} I_i}{n}. \tag{5.4}$$

The sample standard deviation s then is:

$$s = \sqrt{\frac{\sum_{i=1}^{n}(I_i - I_m)^2}{n-1}} \tag{5.5}$$

The proparbility of a measurement lying inside of $[I_m - \tau\sigma, I_m + \tau\sigma]$, according to a gaussian normal distribution $f_{I_m,s}()$, can be expressed as a function of τ. Let $P(\tau\sigma)$ be the proparbility of the measurement I_i lying inside this range, then:

$$P(\tau\sigma) = \int_{I_m-\tau\sigma}^{I_m+\tau\sigma} f_{I_m,s}(I_m)dx. \tag{5.6}$$

We choose to keep all intensity measurements with $P(\tau\sigma) = 95\%$, then $\tau = 1.96$. The measurement I_i lies inside 95% of the gaussian normaldistribution, when:

$$I_m - 1.96s < I_i < I_m + 1.96s. \tag{5.7}$$

Algorithm 1 and 2 show the pseudo code for the implementation of limiting outliers for the neighbour point data set.

Algorithm 1: Distance Check Algorithm

```
foreach point in points do
    if too far or close to laser scanner then
        delete point
end
```

Algorithm 2: Sigma Band Algorithm

```
foreach intensity in points do
    if intensity is invalid then
        delete point, recalculate standard deviation and mean Intensity, and start from
          beginning
end
```

5.6 Calibration and Normalization

Laser scanners come with little to no documentation of how they measure intensity values. Therefore, when using different systems, it is necessary to calibrate the measurements. Scanning reference targets of known reflectance and extracting an intensity relationship between the systems, enables us to compare the measurements with each other.

For standard reflectivity targets of reflectance from 0 % to 100 % documentation of the manufacturer describe a range of 0 to 150 for LIVOX Mid-100 and −20 dB to 0 dB [75] for RIEGL VZ-400. 0dB describes a white Lambertian target (similar to the 99 % spectralon), resulting almost exclusively in intensity measurements below 0db. Intensities higher than 0db indicate retroreflectors as target such as license plates and reflecting foils. Subsequently intensities from

Figure 5.8: Four spectralons in a 3D printed frame. With reflectance 99%, 75%, 50% and 2%

Spectralon Specifications	
Working Temperatures	−80 °C to 350 °C
Thickness	0.55 zoll
Diameter	1.5 zoll
Operating Relative Humidity	5 % - 95 %
Reflective Area Diameter	1.25 inches
Housing Material	Delrin

Table 5.2: Specifications for the Edmund Optics spectralons

151 to 255 recorded by the LIVOX also indicate retroreflectors. The intensity returned by the OUSTER os1-64 is a 16-bit integer and can therefore range from 0 to 65535. This is the total range including retroreflectors.

We use four perfectly diffuse (Lambertian) targets, called spectralons (Figure 5.8). The spectralons specifications are in Tab. 5.2. A Lambertian target follows the Lambertian light reflection (Figure 5.9). The light hitting an extended Lambertian surface is uniformly scattered into the hemisphere [5].

Before starting a test run and scanning samples, we run a calibration process. After manual centre selection of all four spectralons, a node scans them all and puts the intensities into a linear regression algorithm. The node saves the predicted maximum and minimum intensity values for each laser scanner in a CSV file that the analysing node reads when scanning samples.

We use the best fitting line to normalize all sensor systems and their intensities to one range where 0 represents the intensity of a predicted Lambertian reference target with reflectance

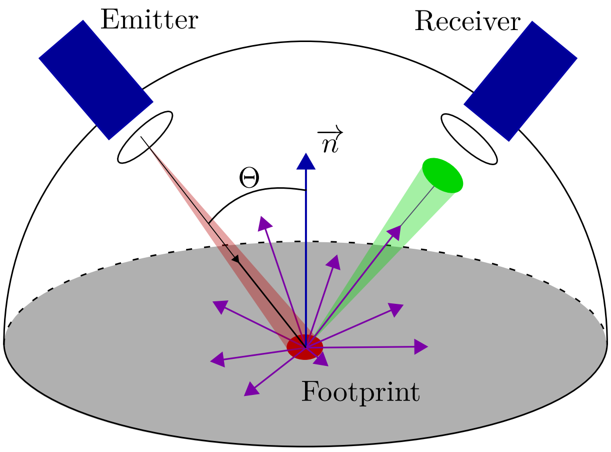

Figure 5.9: Lambertian reflectance, the emitted beam is uniformly scattered into the hemisphere. The purple vectors represent the reflected light and its intensity. With normal vector n and incidence angle Θ. Rebuild according to [5]

0 % an 1 represents a prediction for a target with 100 % reflectance. Let I_i be the value that undergoes normalization and belongs to the range $[I_{\min}, I_{\max}]$, then the normalization formular is defined as

$$\frac{I_i - I_{\min}}{I_{\max} - I_{\min}}. \tag{5.8}$$

With a and b defined as

$$a = \frac{1}{I_{\max} - I_{\min}} \tag{5.9}$$

and

$$b = 1 - a \cdot I_{\max}, \tag{5.10}$$

we brake down the normalization formula 5.8 to keep the recomputations to a minimum to

$$a \cdot I_i + b. \tag{5.11}$$

To calculate the mininma and maxima values, we scan all four spectralons with all three laser scanners. For the measured intensities we find a linear line with coefficient γ and constant c,

$$f(x) = \gamma \cdot I_i + c, \tag{5.12}$$

that the node calculates via regression. The $I_{\min}$ and $I_{\max}$ values we use are the predicted values of the best fitting line from the regression at 0 and 1:

$$f(0) = I_{\min}, f(1) = I_{\max}. \tag{5.13}$$

These represent predicted values for lambertian reflectance targets of reflectance 0 % and 100 %. It is possible for measurements to lie below these predicted targets. In case of non Lambertian reflectance. For equation 5.11 we can save a and b in a class object and dont have to recompute them everytime we are normalizing an intensity value of the same laser scanner. This is beneficial in case we want to scan several targets at once. In future work one might want to analyse a rock wall that consists of different rock type layers. In combination with object detection it is possible to then scan multiple region of interests and identificate their rock types.

The calibrated ranges serve as the upper and lower limits for normalizing the calculated mean intensities on the surfaces of the rocks to a standardized range. This permits us to compare the values of the different laser systems with each other. Even if circumstances like atmosphere or target placement (e.g. the incidence angle) change, we anticipate that these variations will be uniform across all systems and consider their impact to be negligeable.

5.7 Rock samples

The Department for Geography and Geology of the Julius-Maximilians-Universität Würzburg provided us with all samples. All of the samples are of terrestrial origin but represent rock types present on the moon. These are as follows: Anorthosite, Basalt, Dunite, and Ilmenite. Except Ilmenite these types are igneous rock types. Ilmenite is a mineral common as an accessory mineral in igneous rocks [81, Chapter 7]. Basalts are the most significant group of volcanic rocks [81, Chapter 19]. All Anorthosite samples derive from Rkefjord, Rogaland in Norway. The Dunite samples are from Levdalsbygda, Nordfjord in Norway. While the Ilmenite samples come from the Blafjell mines in Rogaland, Norway. The Basalt samples originate from a mine in the Rhön Mountains, Germany. Fig. 5.10 shows all samples side by side. Appendix A contains full depictions of all samples.

Additionally, we covered one sample of each rock type with a thin layer of ice to mimic the way H_2O ice might be present on rock surfaces in lunar caves (Fig. 5.11).

Anorthosite and Dunite are nearly monomineralic stones with little variation in composition. Additionally, the samples available to us show no signs of weathering. Especially Basalt is a compositional varying rock type. The Basalt and Ilmenite, $FeTiO_3$, samples both show signs of weathering that present in the form of brown areas on the sample surface.

For plots and other figures with limited space, we refer to the samples by a short form that does not change throughout the work. Figure 5.10 shows the abbreviations on the respective sample. The capitalized letter stands for the rock type, while the samples are simply numbered from 1 to 3.

We position all laser scanners in a row to each other. From there the laser scanners are not moved during all scans including the calibration scan of the spectralons and the sample scans. Setting the targets on a window sill in front of a working table ensures a wide enough distance

Figure 5.10: All samples we use in this work.

(approximately 2m) for all laser scanners to pick up points on the target surface. Refer to Figure 5.12.

We place the targets in front of a white plate to limit the light coming from the windows. Additionally, we position the targets in the centre of one rosette in the LIVOX point cloud. This gives the highest possible point density on the target surface.

Not changing the relative positions of all scanners to each other makes it possible to compare the ratios of recorded intensities. In theory, all influencing factors like atmosphere, distance, and incidence angle, if changed, change the same amount for all laser systems. So that all ratios stay the same. In a remote robot, all laser scanners must be mounted statically and, when moved, moved together without changing their positions relative to each other.

(a) Anorthosite A1

(b) Basalt B1

(c) Dunite D1

(d) Ilmenite I1

Figure 5.11: Samples with an ice layer on top.

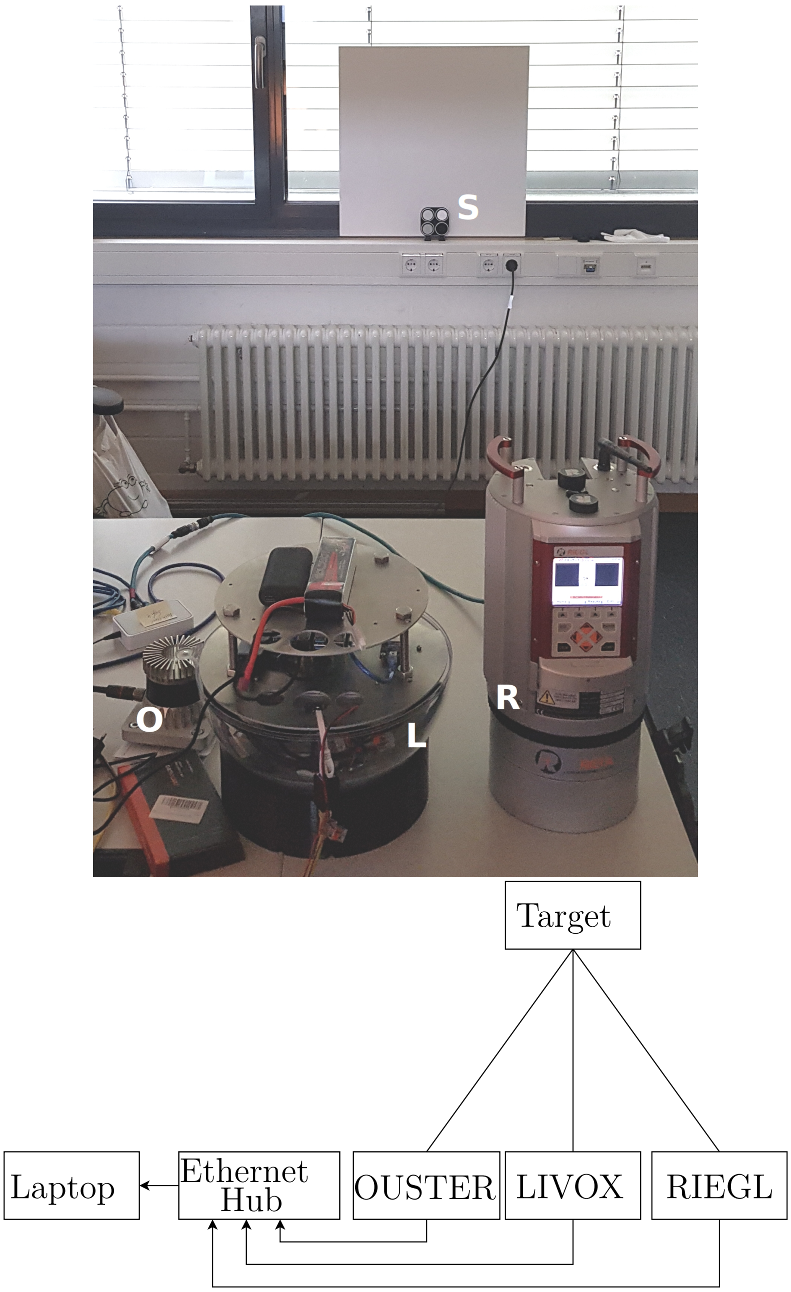

Figure 5.12: Setup structure of test scans as well as the calibration scan. The picture shows the setup in the university room we have available for tests. From left to right OUSTER (O), LIVOX (L, in a DAEDALUS prototype) and RIEGL (R). The target, in this case the spectralons (S), sits on a window sill in front of all sensors. Below is a diagram of the shown setup.

Chapter 6

Experiment and Evaluation

6.1 Results

Calibration

Scanning the spectralons and fitting the measurements to a line through regression enables the determination of a range within which the intensity values for each laser scanner lie. The detected intensity ranges differ from the ranges decribed by the manufacturers (see Section 5.6). The calculated ranges in absolute values are, [-30.1684, 470.4734] for OUSTER, [-11.3593, 69.2977] for LIVOX, and [-16.1683, 3.4348] for RIEGL (Figure 6.1).

For the LIVOX system, the distance calculation for the 2 % spectralon did not work. In the point cloud, most points of the 2 % spectralon lie on a cone towards the laser scanner (refer to Figure 6.2c). For all mean intensity measurements of the LIVOX values, deviation is < 10, while the values are > 10. The exception is the measurement of the 2 % spectralon, the measured mean intensity is < 10 as well, which makes both mean and deviation lie in the same order of magnitude.

Sample Scans

We do a test series scanning all samples from at least two sides. For example, the abbreviation A2-1 refers to another side of sample A2 (which is the second Anorthosite sample).

Measurements of the normalized values show an overall trend for each rock type (Figure 6.5 and 6.6). Two noticeable outliers are I2 (Ilmenite) and B3-1, which is one side of the third Basalt sample. For B3-1 the impact on the ratios is not as significant (Figure 6.7).

When calculating the ratios by dividing the intensity measurements of the LIVOX (905nm) by the OUSTER (865nm) and the RIEGL (1550nm) measurements by the LIVOX (905nm) values (Figure 6.7), the trend of different rock types is even more apparent. Especially the Anorthosite and Dunite samples lie in a relatively small area separated from the other rock types. The I2 outlier has ratios very close to the measured Anorthosite ratios. Also considering the absolute normalized values enables us to rule out the I2 as an Anorthosite sample. The OUSTER measurements for Anorthosite are all well over 35 %, the LIVOX measurements are higher than 20 %, and the RIEGL measurements are above 30 %. For the outlying Ilmenite

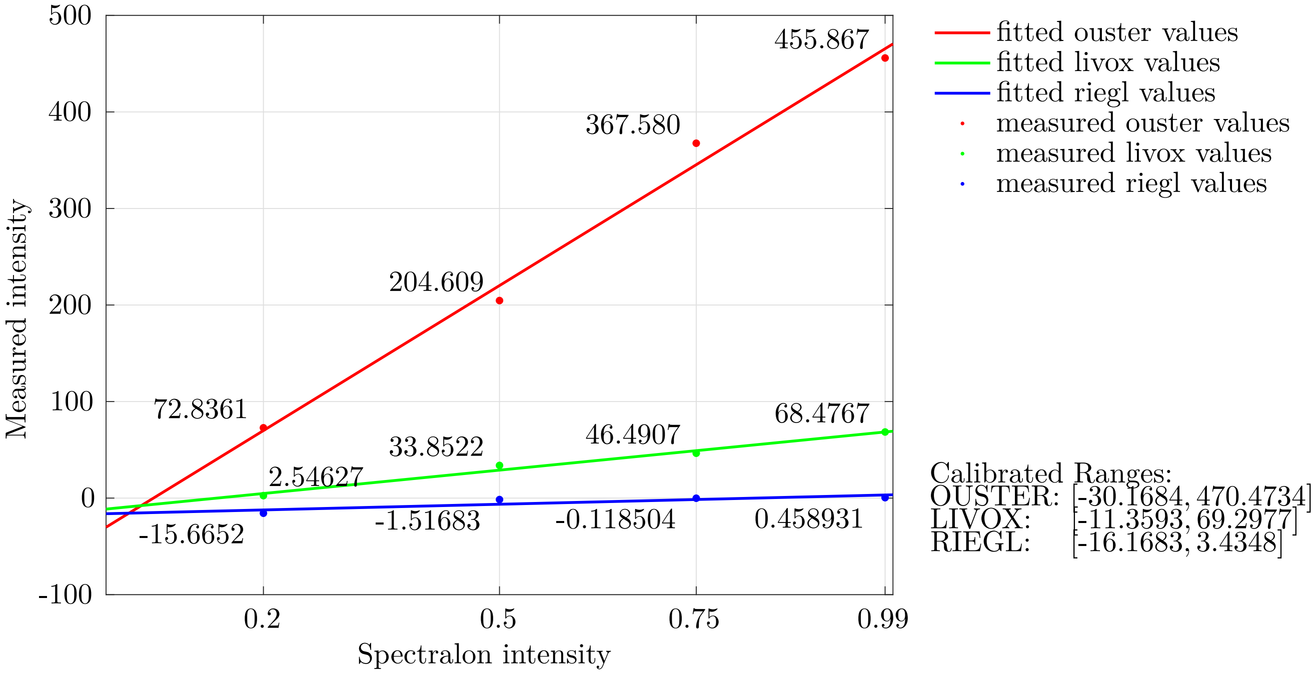

Figure 6.1: Linear regression of measured spectralon values for normalization. Shown values are the measured intensities, each value is rounded to 6 significant digits. In the bottom right calculated ranges are listed.

sample the absolute values are beneath 35 %, 20 %, and 30 %.

The Basalt values and ratios differ the most in consistency (Figure 6.6 and 6.7).

Ice Samples

For all tested samples the samples with H_2O ice show the highest absorption for the wavelength 1550nm (RIEGL) (Figure 6.5). The B1 sample shows up with the highest RIEGL intensity value of all ice samples at 0.12765. All normalized 1550nm measurements are below 13×10^{-2} and the slopes from 905nm to 1550nm for the ice samples are below -4×10^{-5}. The Ilmenite sample covered in ice (I1) shows the lowest intensity value, -0.089053, over all samples at 1550nm and falls into negative space. The measured values for 865nm and 905nm show no noticeable correlation to the underlying material.

6.2 Evaluation

Calibration

The calibrated ranges differ from the ones described by manufacturers because the circumstances and systems are not ideal. Furthermore, the circumstances at the manufacturer facilities, where the systems underwent calibration, vary from the conditions in the test environment. Due to the

(a)

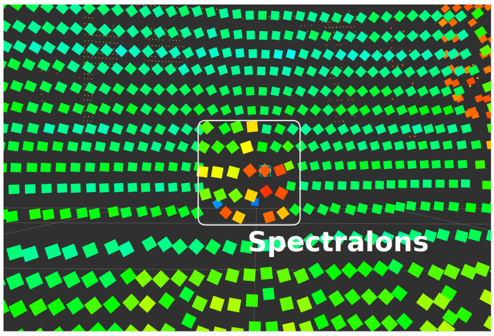

(b) OUSTER point cloud

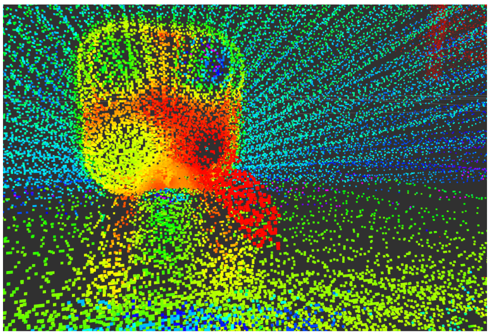

(c) LIVOX point cloud

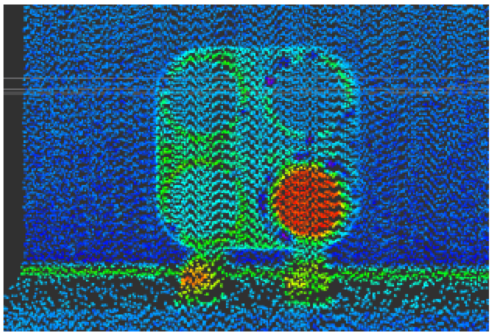

(d) RIEGL point cloud

Figure 6.2: Point clouds of spectralon scans for calibration and an image of the spectralons.

low reflectance of the spectralon, the LIVOX laser system has difficulties detecting the points on the 2 % spectralon correctly.

Rock samples

The Basalt and Ilmenite samples show signs of weathering. All samples have brown areas, these vary in size and prominence.

B3-1 for example is to the human eye significantly lighter than the other main side of the rock (Figure 6.8). The brownish areas on the lighter basalt side cause the intensity measurements to be higher in their absolute value.

Ilmenite is mainly made up of iron (Fe) and titanium (Ti). These two materials reflect light differently. In addition, they vary significantly from Lambertian targets in their reflection. To the human eye, they look "shining" from some angles. The Ilmenite does not reflect light evenly but is dependent on the incidence angle. The orientation of the rock possibly lead to a reflected beam with stronger reflectance received by the RIEGL sensor. Additionally the recorded side is affected by weathering. Both circumstances explain the high measured value for sample I2.

The test scans maintain comparability for all normalized values due to the consistent distance and primary orientation of the samples to the sensors. The surface texture of the natural and unpolished rocks does have impacts on incident angle and therefore reflectance. We kept the overall orientation of the sample surfaces similar throughout the scans. If paired with the optical

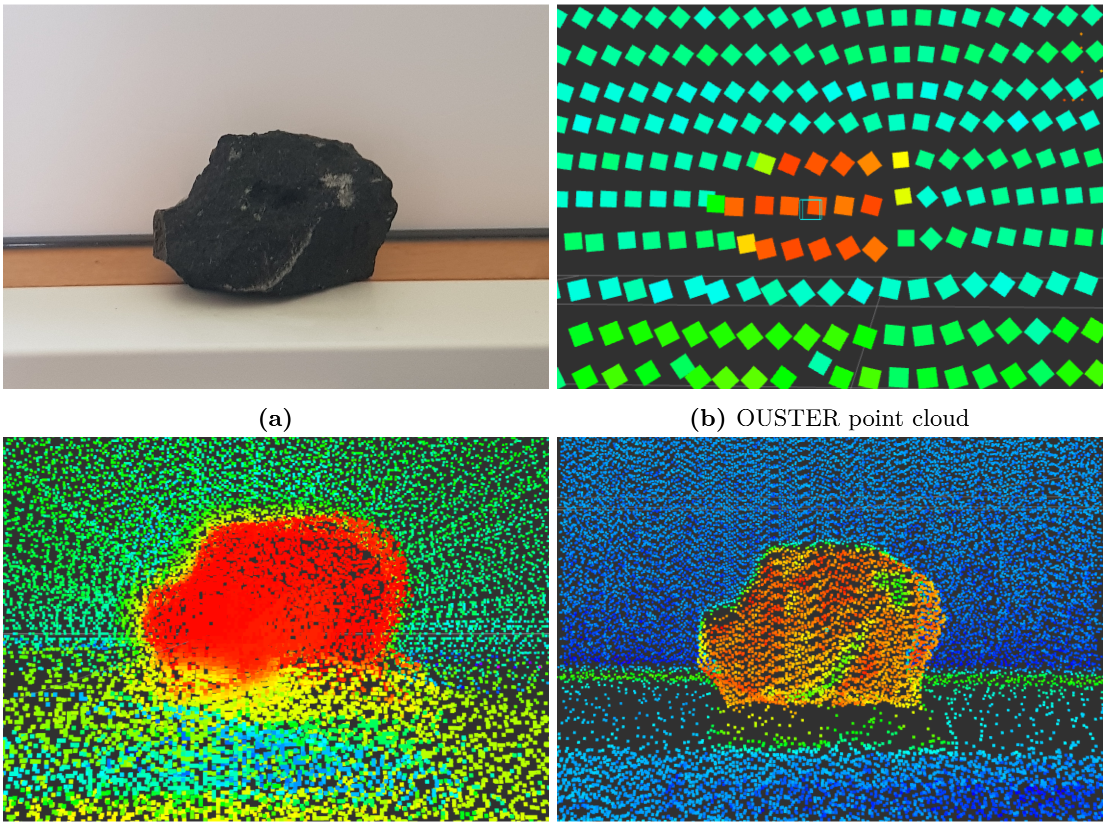

(a) **(b)** OUSTER point cloud

(c) LIVOX point cloud **(d)** RIEGL point cloud

Figure 6.3: Point clouds of Basalt sample B2 besides an image. View of a light vein on the dark sample.

system Gmöhling [32] is inspecting for the DAEDALUS system, the likelihood of identifying outliers correctly is possibly increased. Future research is to identify the possibility of combining both methods.

Dunite is a nearly monomineralic rock [81, Chapter 11] leading to little variation in composition and therefore reflectance. Anorthosite consists of >90Vol.-% plagioclase [81, Chapter 13] and is therefore nearly monomineralic too. These stable conditions reflect in all measurements. The measurements for Dunite and Anorthosite are the most consistent of all. Basalt is a very varying rock type in its composition. This leads to varying measurements for all Basalt samples. The Basalt sample B2 shows a distinct light vein on one of its sides, refer to Figure 6.3. Additionally, the ratios of LIVOX to RIEGL seem to fluctuate less than the OUSTER to LIVOX ratios (Figure 6.7).

Ice samples

As expected the RIEGLS near-infrared wavelength is highly absorbed by water ice. The detection of thin ice layers on top of the rock surfaces is possible.

The area of ice on the Basalt sample scan is the smallest, which results in relatively high

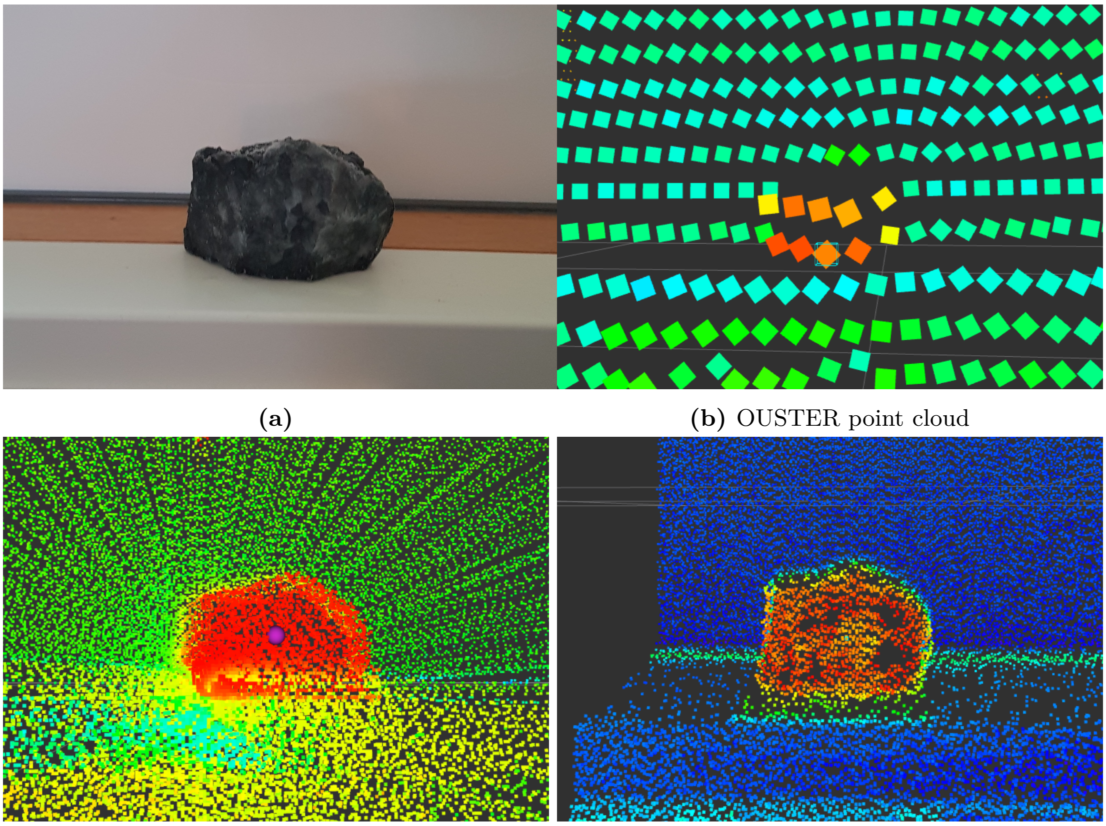

(a) **(b)** OUSTER point cloud

(c) LIVOX point cloud **(d)** RIEGL point cloud

Figure 6.4: Point clouds of Ilmenite sample I1 with H_2O ice besides an image. Missing points in RIEGL point cloud (d) at the highest amounts of water ice. The purple sphere in (c) indicates the selected centre point for calculation of the mean intensity at 905nm.

measurements with the RIEGL sensor. Nevertheless, it is possible to detect the ice on the sample.

The Ilmenite sample covered in ice has the biggest layer of ice. And therefore the normalized RIEGL value is the lowest, lying below 0 because the absorption behaviour is higher than the predicted 0 % Lambertian target.

Gmöhling did experiments with the same ice samples. The ice layer is too thin and seethrough for the optical system to recognize it [82]. Refer to 5.11 for a visual presentation of the ice layers. They are not in the same condition as they were for the unsuccessful optical detection test, due to uncontrollable melting while scanning. Additionally, storing in the freezer changed ice distribution too. In conclusion, the LiDAR system is able to detect ice too thin for the optical system.

On sections with thicker ice layers, the RIEGL cannot pick up points, because the reflected beam portion is too low. On the Ilmenite ice sample (I1) for example, are several missing points in the point cloud (Fig. 6.4). Range specifications for the RIEGL VZ-400 document a minimum range of 1,5m without specifying at which reflectance. We expect the range to be significantly

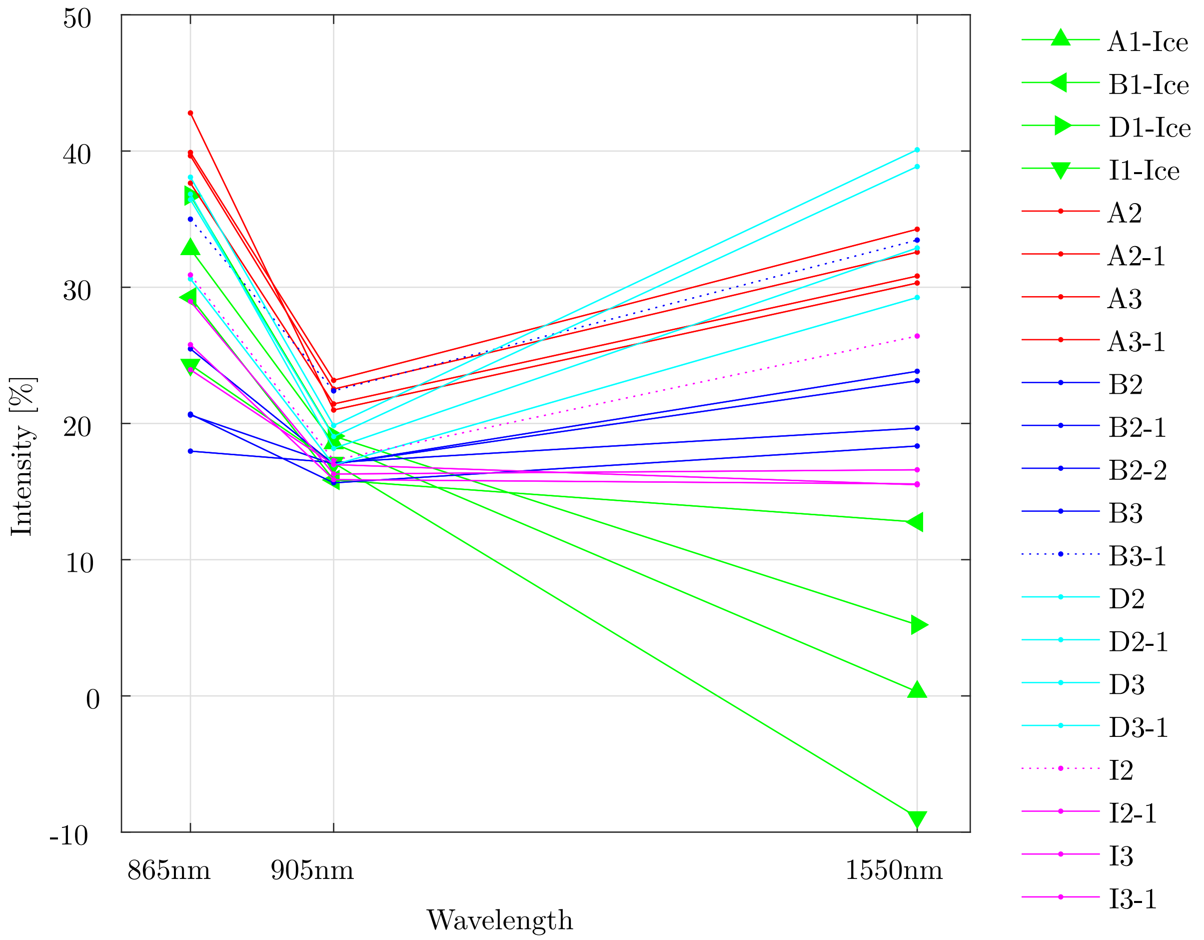

Figure 6.5: LiDAR intensities for terrestrial rock samples taken with an OUSTER (865nm), LIVOX (905nm), and RIEGL(1550nm) of the types Anorthosite (A1, A2, A2-1, A3, A3-1), Basalt (B1, B2, B2-1, B2-2, B3), Dunite (D1, D2, D2-1, D3, D3-1) and Ilmenite (I1, I2-1, I3, I3-1). A1, B1, D1 and I1 are covered with a thin H_2O ice layer. Dotted lines (B3-1, I2) are of dislocated sample measurements.

lower for H_2O ice, due to its high absorption of 1550nm wavelengths. Looking at missing points in an otherwise dense point cloud, therefore, is an additional indicator of ice.

The detection of the underlying rock type is not possible with our methods, if desired further research and improvement has to be done.

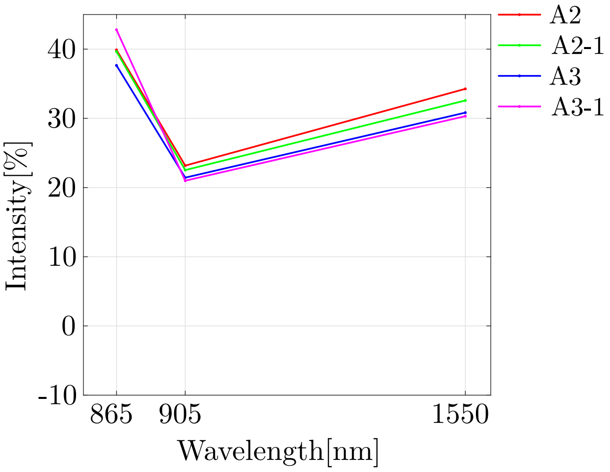

(a) anorthosite samples

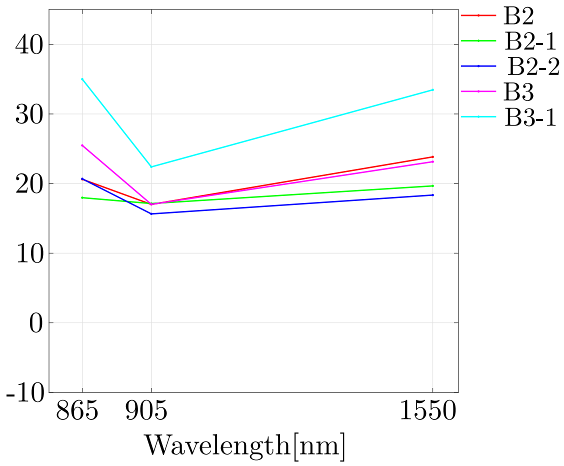

(b) basalt samples

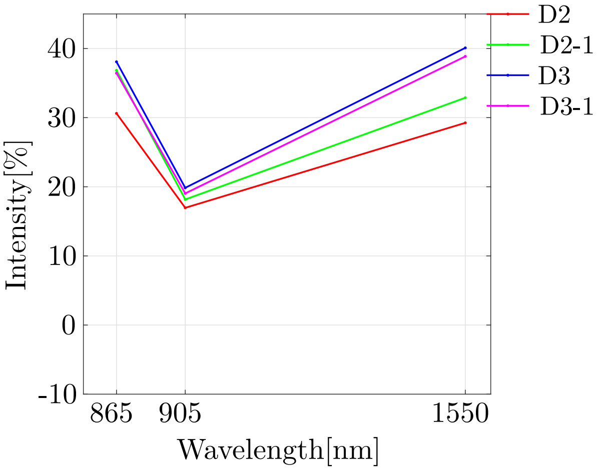

(c) dunite samples

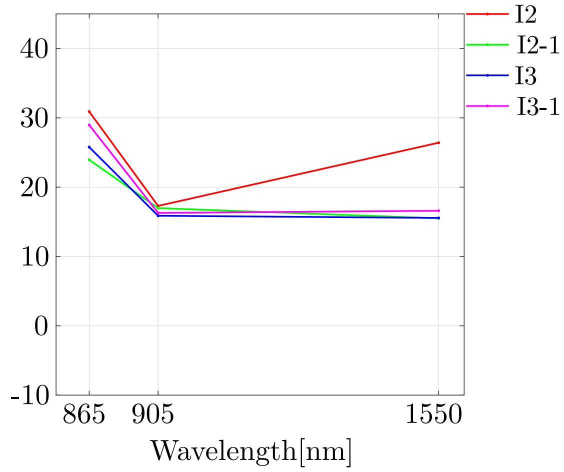

(d) ilmenite samples

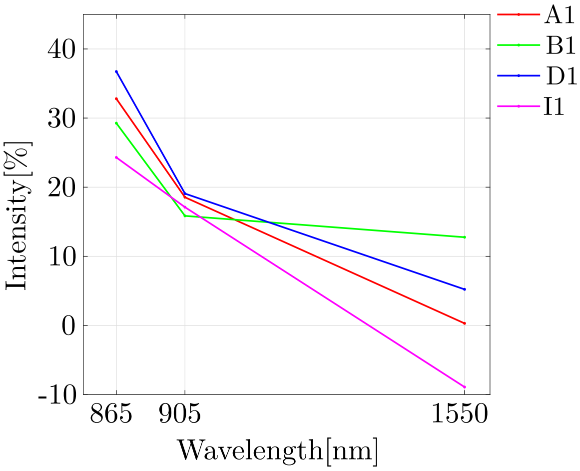

(e) H_2O ice samples

Figure 6.6: LiDAR intensities for terrestrial rock samples taken with an OUSTER (865nm), LIVOX (905nm), and RIEGL(1550nm) of the types Anorthosite (A2, A2-1, A3, A3-1) (a), Basalt (B2, B2-1, B2-2, B3, B3-1) (b), Dunite (D2, D2-1, D3, D3-1) (c) and Ilmenite (I2, I2-1, I3, I3-1) (e). As well as all Ice samples (Anorthosite A1, Basalt B1, Dunite D1, Ilmenite I1) (e).

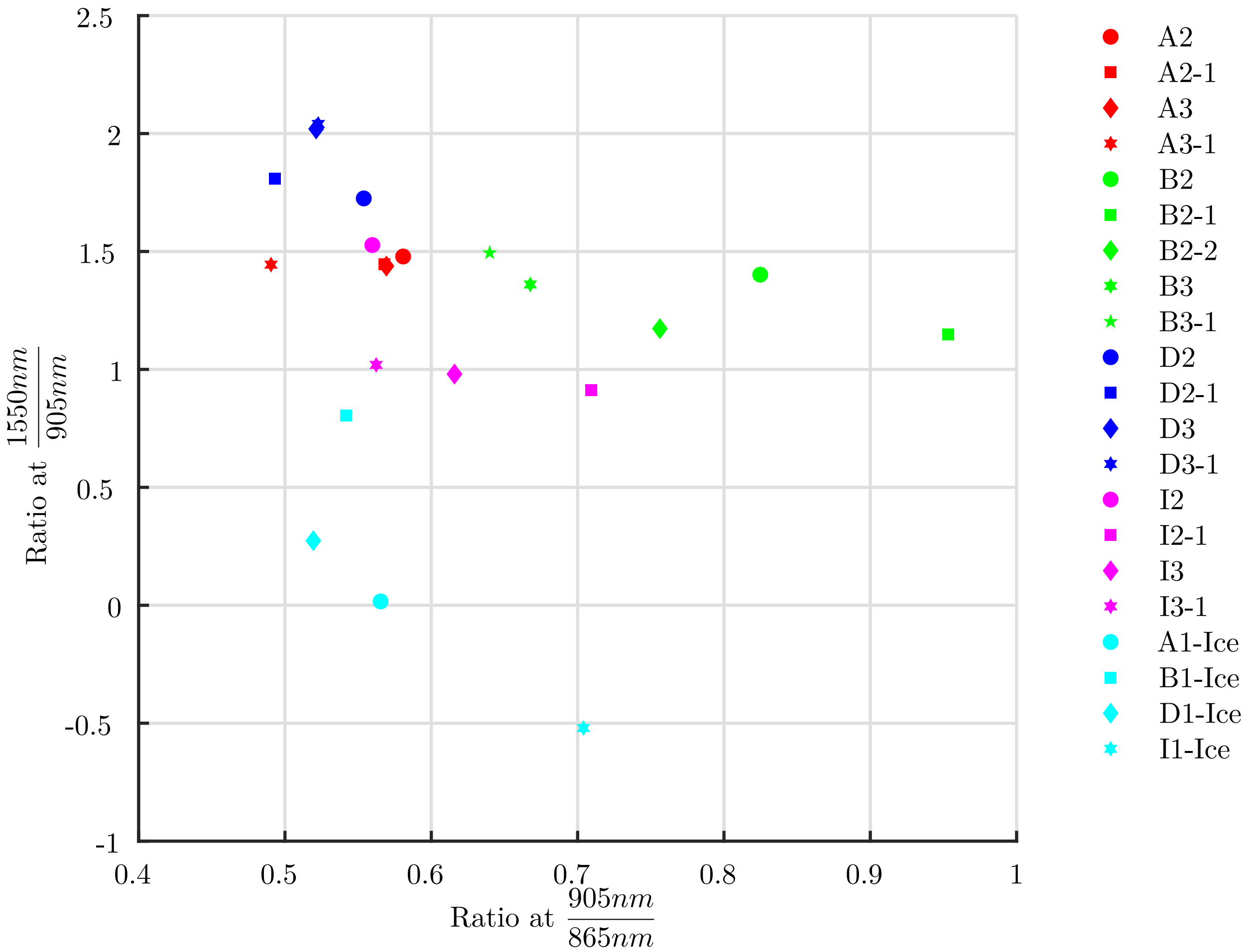

Figure 6.7: LiDAR intensities for terrestrial rock samples plotted as ratios. Taken with an OUSTER (865nm), LIVOX (905nm), and RIEGL(1550nm) of the types Anorthosite (A1, A2, A2-1, A3, A3-1), Basalt (B1, B2, B2-1, B2-2, B3), Dunite (D1, D2, D2-1, D3, D3-1) and Ilmenite (I1, I2-1, I3, I3-1). A1, B1, D1 and I1 are covered with a thin H_2O ice layer.

(a) (b)

Figure 6.8: The two main sides of Basalt sample three. Side (b) is noticeably lighter than (a).

Chapter 7

Conclusion

In this work, we show that using three laser scanners does show potential in distinguishing rock types. The aim of this work is to get a first impression and evaluation of whether LiDAR intensity is suitable to distinguish between surface materials, specifically rock types in moon caves. The main goal was a simple method, mainly without performing a correction for true reflectance. As well as to test this on available LiDAR systems, with respect to future investment for the DAEDALUS project. This work gives an impression on whether it is feasible to go further into detail and refine the method for an autonomous system, like the spherical robot from DAEDALUS.

The method described in this work simply takes points on the sample surface, forms a mean intensity, and normalizes it to the same range for all laser scanners. To calculate the normalization parameters one only needs to scan at least three reference targets with known reflectance (e.g. spectralons) with all laser scanners. The laser scanners have to be static in relation to each other. If they move, they move together. For example by being mounted fixed on the same robot. So that variables, like distance, change in the same amounts for all laser scanners.

We performed tests with rock samples of types present on the moon, Basalt, Ilmenite, Dunite, Anorthosite. All scanned rock samples behaved as expected. Anorthosite and Dunite have very consistent values and relations as they are monomineralic rocks. Ilmenite, $FeTiO_3$, has a high outlier due to its metallic nature and non-Lambertian reflectance. And the Basalt measurements vary all over due to Basalt having a very varying composition. Ice shows a high absorption for 1550nm and can be detected in layers that are too thin for the optical system [82]. With our current method, it is not possible to detect the rock type beneath the ice layer. Further research is needed to characterize the full behaviour of thin ice layers and if the detection of the material below is possible.

The presented method relies on systems significantly cheaper than hyperspectral sensors. The manual centre point selection we implement is prone to human error, improving on transformation or automatic object or region of interest detection enables a higher autonomy. This possibly limits background points not belonging to the sample even further. The methods of limiting radius, distances and sigma band are prone to include measurements not from the sample surface. When continuing to work with sample sizes smaller than 20cm using a sensor with higher precision than the OUSTER os1-64 is beneficial. The limited unique points are inefficient for working with small samples for the identification of the material. For future research, we propose to use a wider range of wavelengths. The 865nm is close to the 905nm. Using more distinct wavelengths improves discrimination possibilities. In addition, further research is needed to grow a database and define bounds for rock types to enable automatic identification. Field research will refine our methods and enable the discrimination of a wider spectrum of rock types. As well as increase the probability of identifying the sample correctly. In the future, LiDAR intensity holds the potential to distinguish between a wide variety of materials. This benefits lava tube exploration in multiple ways. The analysis of lava emplacement, volcanic layering, and composition as well as an understanding of the geology and mineralogy. We expect the spectral signatures of rocks in the subsurface to be more stable because they are less affected by space weathering.

Bibliography

[1] NASA. Gateway. https://www.nasa.gov/gateway/overview. Accessed: June 22 2023.

[2] NASA. Artemis. https://www.nasa.gov/specials/artemis/. Accessed: June 22 2023.

[3] ESA. Argonaut. https://www.esa.int/Science_Exploration/Human_and_Robotic_Exploration/Exploration/Argonaut. Accessed: June 22 2023.

[4] New Views of Lunar Pits. https://www.nasa.gov/mission_pages/LRO/multimedia/lroimages/lroc-20100914_lunarpits.html, 2010. Accessed: June 23 2023.

[5] Kai Tan and Xiaojun Cheng. Surface reflectance retrieval from the intensity data of a terrestrial laser scanner. *J. Opt. Soc. Am. A*, 33(4):771–778, Apr 2016.

[6] Yuwei Chen, Changhui Jiang, Juha Hyyppä, Shi Qiu, Zheng Wang, Mi Tian, Wei Li, Eetu Puttonen, Hui Zhou, Ziyi Feng, Yuming Bo, and Zhijie Wen. Feasibility study of ore classification using active hyperspectral lidar. *IEEE Geoscience and Remote Sensing Letters*, 15(11):1785–1789, 2018.

[7] Nancy Atkinson. Lava Tubes on the Moon Maintain Comfortable Room Temperatures Inside. https://www.universetoday.com/156932/lava-tubes-on-the-moon-maintain-comfortable-room-temperatures-inside/, 2022. Accessed: June 22 2023.

[8] Bill Steigerwald. NASA's LRO Finds Lunar Pits Harbor Comfortable Temperatures. https://www.nasa.gov/feature/goddard/2022/lro-lunar-pits-comfortable, 2022. Accessed: June 23 2023.

[9] John Mylroie. Caves in space. *Journal of Cave and Karst Studies*, 81(1):25–32, March 2019.

[10] Timothy N Titus, CM Phillips-Lander, PJ Boston, JJ Wynne, and L Kerber. Planetary cave exploration progresses. *Eos, Earth and Space Science News*, 101, December 2020.

[11] Timothy N. Titus, J. Judson Wynne, Michael J. Malaska, Ali-akbar Agha-Mohammadi, Peter B. Buhler, James W. Alexander, E. Calvin andAshley, Armando Azua-Bustos, Penelope J. Boston, Debra L. Buczkowski, Leroy Chiao, Glen E. Cushing, John DeDecker, Pablo de Leon, Cansu Demirel-Floyd, Jo De Waele, Alberto G. Fairen, Amos Frumkin, Gary L. Harris, Heather Jones, Laura H. Kerber, Erin J. Leonard, Richard J. Leveille, Kavya Manyapu, Matteo Massironi, Ana Z. Miller, John E. Mylroie, Bogdan P. Onac,

Scott Parazynski, Cynthia B. Phillips, Charity M. Phillips-Lander, Thomas H. Prettyman, Haley M. Sapers, Francesco Sauro, Norbert Schorghofer, Dirk Schulze-Makuch, Jennifer E. Scully, Kyle Uckert, Robert V. Wagner, William L. Whittaker, Kaj E. Williams, and Uland Y. Wong. A roadmap for planetary caves science and exploration. *Nature Astronomy*, 5:524–525, June 2021.

[12] Angelo Pio Rossi, Francesco Maurelli, Vikram Unnithan, Hendrik Dreger, Kedus Mathewos, Nayan Pradhan, Dan-Andrei Corbeanu, Riccardo Pozzobon, Matteo Massironi, Sabrina Ferrari, Claudia Pernechele, Lorenzo Paoletti, Emanuele Simioni, Pajola Maurizio, Tommaso Santagata, Dorit Borrmann, Andreas Nüchter, Anton Bredenbeck, Jasper Zevering, Fabian Arzberger, and Camilo Andres Reyes Mantilla. Daedalus - descent and exploration in deep autonomy of lava underground structures. Technical Report 21, Institut für Informatik, 2021.

[13] P.J. Boston. Bubbles in the rocks: human use of caves on the moon and mars, 25 years on. In *Proceedings of the 4th International Planetary Caves Conference* [83]. Abstract Nr. 1082.

[14] Tyler Horvath, Paul O. Hayne, and David A. Paige. Thermal and illumination environments of lunar pits and caves: Models and observations from the diviner lunar radiometer experiment. *Geophysical Research Letters*, 49(14):e2022GL099710, 2022. e2022GL099710 2022GL099710.

[15] Pascal Lee. Planetary caves: a rational for their top priority in astrobiology, mars, and "moon to mars" science and exploration. In *Proceedings of the 4th International Planetary Caves Conference* [83]. Abstract Nr. 1076.

[16] Jasper Zevering. TLDR Robot Telescopic Linear Driven Rotation Robot - A Locomotion Approach for Spherical Robots. Master's thesis, Julius-Maximilian University of Würzburg, 2021.

[17] ESA. ESA plans mission to explore lunar caves. `https://www.esa.int/Enabling_Support/Preparing_for_the_Future/Discovery_and_Preparation/ESA_plans_mission_to_explore_lunar_caves`. Accessed: May 3 2023.

[18] ESA. Seeking innovative ideas for exploring lunar caves. `https://www.esa.int/Enabling_Support/Preparing_for_the_Future/Discovery_and_Preparation/Seeking_innovative_ideas_for_exploring_lunar_caves`. Accessed: May 3 2023.

[19] ESA. Lunar scientists and engineers design Moon cave explorer. `https://www.esa.int/Enabling_Support/Preparing_for_the_Future/Discovery_and_Preparation/Lunar_scientists_and_engineers_design_Moon_cave_explorer`. Accessed: May 3 2023.

[20] Pablo F. Miaja, Fermin Navarro-Medina, Daniel G. Aller, Germán León, Alejandro Camanzo, Carlos Manuel Suarez, Francisco G. Alonso, Diego Nodar, Francesco Sauro, Massimo Bandecchi, Loredana Bessone, Fernando Aguado-Agelet, and Manuel Arias.

Robocrane: A system for providing a power and a communication link between lunar surface and lunar caves for exploring robots. *Acta Astronautica*, 192:30–46, 2022.

[21] Luca Penasa. *Laserscanner cyclostratigraphy, A remote sensing approach for the extraction of long time series from large outcrops*. PhD thesis, Università degli Studi di Padova, 2015.

[22] R. N. Clark and T. L. Roush. Reflectance spectroscopy: quantitative analysis techniques for remotesensing applications. *Journal of Geophyisical Research*, 89:6329–6340, July 1984.

[23] A. Pesci, G. Teza, and G. Ventura. Remote sensing of volcanic terrains by terrestrial laser scanner: preliminary reflectance and rgb implications for studying vesuvius crater (italy), 2008.

[24] Marco Franceschi, Giordano Teza, Nereo Preto, Arianna Pesci, Antonio Galgaro, and Stefano Girardi. Discrimination between marls and limestones using intensity data from terrestrial laser scanner. *ISPRS Journal of Photogrammetry and Remote Sensing*, 64(6):522–528, 2009.

[25] Preston Hartzell, Craig Glennie, Kivanc Biber, and Shuhab Khan. Application of multispectral lidar to automated virtual outcrop geology. *ISPRS Journal of Photogrammetry and Remote Sensing*, 88:147–155, 2014.

[26] Leonardo Campos Inocencio, Mauricio Roberto Veronez, Francisco Manoel Wohnrath Tognoli, Marcelo Kehl de Souza, Reginaldo Maced\undefined onio da Silva, Luiz Gonzaga Jr, and C\undefined esar Leonardo Blum Silveira. Spectral Pattern Classification in Lidar Data for Rock Identification in Outcrops. *The Scientific World Journal*, 2014:1–10, 2014.

[27] D. Burton, D. B. Dunlap, L. J. Wood, and P. P. Flaig. Lidar Intensity as a Remote Sensor of Rock Properties. *Journal of Sedimentary Research*, 81(5):339–347, may 1 2011.

[28] Kim Moonjoo, Lee Sudeuk, and Jeon Seokwon. Analysis of parameters affecting lidar intensity on rock. *Tunnel and Underground Space*, 30(4):417–431, 08 2020.

[29] Liping Li, Lanyu Cui, Hongliang Liu, Chengshuai Qin, Jie Hu, and Mingguang Zhang. A method of tunnel critical rock identification and stability analysis based on a laser point cloud. *Arabian Journal of Geosciences*, 13(13), jun 24 2020.

[30] Mohammed Idrees and Biswajeet Pradhan. Geo-structural and stability assessment of cave using rock surface discontinuity extracted from terrestrial laser scanning point cloud. *Journal of Rock Mechanics and Geotechnical Engineering*, 10, 04 2018.

[31] Kenneth Lymer. Image processing and visualisation of rock art laser scans from loups's hill, county durham. *Digital Applications in Archaeology and Cultural Heritage*, 2(2):155–165, 2015. Digital imaging techniques for the study of prehistoric rock art.

[32] Max Gmöhling. Non-invasive identification of lunar rocks with optical cameras. Bachelor's thesis, Julius-Maximilian University of Würzburg, 2023.

[33] Tuomo Malkamäki, Sanna Kaasalainen, and Julian Ilinca. Portable hyperspectral lidar utilizing 5 ghz multichannel full waveform digitization. *Opt. Express*, 27(8):A468–A480, Apr 2019.

[34] Teemu Hakala, Juha Suomalainen, Sanna Kaasalainen, and Yuwei Chen. Full waveform hyperspectral lidar for terrestrial laser scanning. *Opt. Express*, 20(7):7119–7127, Mar 2012.

[35] R. Gaulton, F.M. Danson, F.A. Ramirez, and O. Gunawan. The potential of dual-wavelength laser scanning for estimating vegetation moisture content. *Remote Sensing of Environment*, 132:32–39, 2013.

[36] Jan U.H. Eitel, Troy S. Magney, Lee A. Vierling, and GÃ¼nter Dittmar. Assessment of crop foliar nitrogen using a novel dual-wavelength laser system and implications for conducting laser-based plant physiology. *ISPRS Journal of Photogrammetry and Remote Sensing*, 97:229–240, 2014.

[37] Baru Chung, Jaehyung Yu, Lei Wang, Nam Hoon Kim, Bum Han Lee, Sangmo Koh, and Sangin Lee. Detection of magnesite and associated gangue minerals using hyperspectral remote sensing - a laboratory approach. *Remote Sensing*, 12(8):1325, Apr 2020.

[38] Jie Bai, Shuai Gao, Zheng Niu, Changsai Zhang, Kaiyi Bi, Gang Sun, and Yanru Huang. A novel algorithm for leaf incidence angle effect correction of hyperspectral lidar. *IEEE Transactions on Geoscience and Remote Sensing*, 60:1–9, 2022.

[39] Kaiyi Bi, Shuai Gao, Zheng Niu, Changsai Zhang, and Ni Huang. Estimating leaf chlorophyll and nitrogen contents using active hyperspectral lidar and partial least square regression method. *Journal of Applied Remote Sensing*, 13:1, 08 2019.

[40] Kaiyi Bi, Shunfu Xiao, Shuai Gao, Changsai Zhang, Ni Huang, and Zheng Niu. Estimating vertical chlorophyll concentrations in maize in different health states using hyperspectral lidar. *IEEE Transactions on Geoscience and Remote Sensing*, 58(11):8125–8133, 2020.

[41] Peilun Hu, Yuwei Chen, Changhui Jiang, Qinan Lin, Wei Li, Jianbo Qi, Linfeng Yu, Hui Shao, and Huaguo Huang. Spectral observation and classification of typical tree species leaves based on indoor hyperspectral lidar. *JOURNAL OF INFRARED AND MILLIMETER WAVES*, 39:372–380, 06 2020.

[42] Jean-Baptiste Sirven, Béatrice Sallé, Patrick Mauchien, Jean-Luc Lacour, Sylvestre Maurice, and Gérard Manhès. Feasibility study of rock identification at the surface of Mars by remote laser-induced breakdown spectroscopy and three chemometric methods. *Journal of Analytical Atomic Spectrometry*, 22(12):1471, 2007.

[43] Juntao Yang, Zhizhong Kang, Ze Yang, Juan Xie, Bin Xue, Jianfeng Yang, and Jinyou Tao. A Laboratory Open-Set Martian Rock Classification Method Based on Spectral Signatures. *IEEE Transactions on Geoscience and Remote Sensing*, 60:1–15, 2022.

[44] Liangchen Jia, Xiangfeng Liu, Weiming Xu, Xuesen Xu, Luning Li, Zhicheng Cui, Ziyi Liu, and Rong Shu. Initial drift correction and spectral calibration of marscode laser-induced breakdown spectroscopy on the zhurong rover. *Remote Sensing*, 14(23):5964, Nov 2022.

[45] K. A. Farley, K. M. Stack, D. L. Shuster, B. H. N. Horgan, J. A. Hurowitz, J. D. Tarnas, J. I. Simon, V. Z. Sun, E. L. Scheller, K. R. Moore, S. M. McLennan, P. M. Vasconcelos, R. C. Wiens, A. H. Treiman, L. E. Mayhew, O. Beyssac, T. V. Kizovski, N. J. Tosca, K. H. Williford, L. S. Crumpler, L. W. Beegle, J. F. Bell, B. L. Ehlmann, Y. Liu, J. N. Maki, M. E. Schmidt, A. C. Allwood, H. E. F. Amundsen, R. Bhartia, T. Bosak, A. J. Brown, B. C. Clark, A. Cousin, O. Forni, T. S. J. Gabriel, Y. Goreva, S. Gupta, S.-E. Hamran, C. D. K. Herd, K. Hickman-Lewis, J. R. Johnson, L. C. Kah, P. B. Kelemen, K. B. Kinch, L. Mandon, N. Mangold, C. Quantin-Nataf, M. S. Rice, P. S. Russell, S. Sharma, S. Siljeström, A. Steele, R. Sullivan, M. Wadhwa, B. P. Weiss, A. J. Williams, B. V. Wogsland, P. A. Willis, T. A. Acosta-Maeda, P. Beck, K. Benzerara, S. Bernard, A. S. Burton, E. L. Cardarelli, B. Chide, E. Clavé, E. A. Cloutis, B. A. Cohen, A. D. Czaja, V. Debaille, E. Dehouck, A. G. Fairén, D. T. Flannery, S. Z. Fleron, T. Fouchet, J. Frydenvang, B. J. Garczynski, E. F. Gibbons, E. M. Hausrath, A. G. Hayes, J. Henneke, J. L. Jørgensen, E. M. Kelly, J. Lasue, S. Le Mouélic, J. M. Madariaga, S. Maurice, M. Merusi, P.-Y. Meslin, S. M. Milkovich, C. C. Million, R. C. Moeller, J. I. Nunez, A. M. Ollila, G. Paar, D. A. Paige, D. A. K. Pedersen, P. Pilleri, C. Pilorget, P. C. Pinet, J. W. Rice, C. Royer, V. Sautter, M. Schulte, M. A. Sephton, S. K. Sharma, S. F. Sholes, N. Spanovich, M. St. Clair, C. D. Tate, K. Uckert, S. J. VanBommel, A. G. Yanchilina, and M.-P. Zorzano. Aqueously altered igneous rocks sampled on the floor of jezero crater, mars. *Science*, 377(6614):eabo2196, 2022.

[46] Elli Angelopoulou and John R. Wright Jr. Laser scanner technology. June 1999.

[47] Lars Lindner. Laser scanners. In *Developing and Applying Optoelectronics in Machine Vision*. IGI Global, 2017.

[48] LIVOX Tech. Livox Wiki. `https://livox-wiki-en.readthedocs.io`. Accessed: May 22 2023.

[49] Zheng Liu, Fu Zhang, and Xiaoping Hong. Low-cost retina-like robotic lidars based on incommensurable scanning. *IEEE/ASME Transactions on Mechatronics*, PP:1–1, 02 2021.

[50] Alireza G. Kashani, Michael J. Olsen, Christopher E. Parrish, and Nicholas Wilson. A review of lidar radiometric processing: From ad hoc intensity correction to rigorous radiometric calibration. *Sensors*, 15(11):28099–28128, 2015.

[51] Nathan Sanchiz-Viel, Estelle Bretagne, El Mustapha Mouaddib, and Pascal Dassonvalle. Radiometric correction of laser scanning intensity data applied for terrestrial laser scanning. *ISPRS Journal of Photogrammetry and Remote Sensing*, 172:1–16, 2021.

[52] Weichen Dai, Shenzhou Chen, Zhaoyang Huang, Yan Xu, and Da Kong. Lidar intensity completion: Fully exploiting the message from lidar sensors. *Sensors*, 22(19):7533, Oct 2022.

[53] Yi-Ting Cheng, Yi-Chun Lin, and Habib Ayman. Generalized lidar intensity normalization and its positive impact on geometric and learning-based lane marking detection. *Remote Sensing*, 14:4393, 09 2022.

[54] Xiaolu Li, Yuhan Shang, Baocheng Hua, Ruiqin Yu, and Yuntao He. Lidar intensity correction for road marking detection. *Optics and Lasers in Engineering*, 160:107240, 2023.

[55] Bernhard Höfle and Norbert Pfeifer. Correction of laser scanning intensity data: Data and model-driven approaches. *ISPRS Journal of Photogrammetry and Remote Sensing*, 62(6):415–433, 2007.

[56] Wai Yeung Yan, Ahmed Shaker, Ayman Habib, and Ana Paula Kersting. Improving classification accuracy of airborne lidar intensity data by geometric calibration and radiometric correction. *ISPRS Journal of Photogrammetry and Remote Sensing*, 67:35–44, 2012.

[57] Qiong Ding, Wu Chen, Bruce King, Yanxiong Liu, and Guoxiang Liu. Combination of overlap-driven adjustment and phong model for lidar intensity correction. *ISPRS Journal of Photogrammetry and Remote Sensing*, 75:40–47, 2013.

[58] Wei Fang, Xianfeng Huang, Fan Zhang, and Deren Li. Intensity correction of terrestrial laser scanning data by estimating laser transmission function. *IEEE Transactions on Geoscience and Remote Sensing*, 53(2):942–951, 2015.

[59] Teng Xu, Lijun Xu, Bingwei Yang, Xiaolu Li, and Junen Yao. Terrestrial laser scanning intensity correction by piecewise fitting and overlap-driven adjustment. *Remote Sensing*, 9(11), 2017.

[60] Teng Xu, Lijun Xu, Bingwei Yang, Xiaolu Li, and Junen Yao. Terrestrial laser scanning intensity correction by piecewise fitting and overlap-driven adjustment. *Remote Sensing*, 9:1090, 10 2017.

[61] Qiong Wu, Ruofei Zhong, Pinliang Dong, You Mo, and Yunxiang Jin. Airborne lidar intensity correction based on a new method for incidence angle correction for improving land-cover classification. *Remote Sensing*, 13(3):511, Feb 2021.

[62] Francesco Pirotti, Alberto Guarnieri, and Antonio Vettore. State of the art of ground and aerial laser scanning technologies for high-resolution topography of the earth surface. *European Journal of Remote Sensing*, 46(1):66–78, 2013.

[63] Sooyoung Kim, Robert J. McGaughey, Hans-Erik Andersen, and Gerard Schreuder. Tree species differentiation using intensity data derived from leaf-on and leaf-off airborne laser scanner data. *Remote Sensing of Environment*, 113(8):1575–1586, 2009.

[64] J. Heinzel and M. Huber. Tls field data based intensity correction for forest environments. *ISPRS - International Archives of the Photogrammetry, Remote Sensing and Spatial Information Sciences*, XLI-B8:643–649, 06 2016.

[65] Michael Oren and Shree K. Nayar. Generalization of lambert's reflectance model. In *Proceedings of the 21st Annual Conference on Computer Graphics and Interactive Techniques*, SIGGRAPH '94, pages 239–246, New York, NY, USA, 1994. Association for Computing Machinery.

[66] Dario Carrea, Antonio Abellan, Florian Humair, Battista Matasci, Marc-Henri Derron, and Michel Jaboyedoff. Correction of terrestrial lidar intensity channel using oren-nayar reflectance model: An application to lithological differentiation. *ISPRS Journal of Photogrammetry and Remote Sensing*, 113:17–29, 2016.

[67] Michaela Nováková, Michal Gallay, Jozef Supinsky, E. Ferre, Riccardo Asti, Michel de Saint Blanquat, Flora Bajolet, and Patrick Sorriaux. Correcting laser scanning intensity recorded in a cave environment for high-resolution lithological mapping: A case study of the gouffre georges, france. *Remote Sensing of Environment*, 280:113210, 10 2022.

[68] Kai Tan and Xiaojun Cheng. Specular reflection effects elimination in terrestrial laser scanning intensity data using phong model. *Remote Sensing*, 9:853, 08 2017.

[69] Dimitrios Bolkas. Terrestrial laser scanner intensity correction for the incidence angle effect on surfaces with different colours and sheens. *International Journal of Remote Sensing*, 40:1–21, 04 2019.

[70] Kai Tan, Jin Chen, Weiwei Qian, Weiguo Zhang, Fang Shen, and Xiaojun Cheng. Intensity data correction for long-range terrestrial laser scanners: A case study of target differentiation in an intertidal zone. *Remote Sensing*, 11:331, 02 2019.

[71] Wolfgang Wagner. Radiometric calibration of small-footprint full-waveform airborne laser scanner measurements: Basic physical concepts. *ISPRS Journal of Photogrammetry and Remote Sensing*, 65(6):505–513, 2010. ISPRS Centenary Celebration Issue.

[72] Ouster, Inc. Ouster Sensor Documentation. `https://static.ouster.dev/sensor-docs/`. Accessed: March 28 2023.

[73] Ouster, Inc. *OS1 Mid-Range High-Resolution Imaging Lidar*, 2023. Datasheet. [Online]. Available: `https://static.ouster.dev/sensor-docs/hw_user_manual/hw_common_sections_OS0/os0-overview.html#os0-rev7`. Accessed: June 23 2023.

[74] Ouster, Inc. *OS1 Hardware User Manual*, 2023. [Online]. Available: `https://static.ouster.dev/sensor-docs/hw_user_manual_OS1/hw_common_sections_OS1/os1-overview.html#os1-rev7`. Accessed: June 23 2023.

[75] RIEGL LASER MEASUREMENT SYSTEMS. *RIEGL VZ-400 Laser Scanners*, 03 2009. [Online]. Available: `http://www.riegl.com/uploads/tx_pxpriegldownloads/RIEGL_VZ-400_News_03-2009.pdf`. Accessed: June 06 2023.

[76] Kim Calders, Mathias I. Disney, John Armston, Andrew Burt, Benjamin Brede, Niall Origo, Jasmine Muir, and Joanne Nightingale. Evaluation of the range accuracy and the radiometric calibration of multiple terrestrial laser scanning instruments for data interoperability. *IEEE Transactions on Geoscience and Remote Sensing*, 55(5):2716–2724, 2017.

[77] ROS Introduction. `http://wiki.ros.org/ROS/Introduction`. Accessed: March 23 2023.

[78] ROS Concepts. `http://wiki.ros.org/ROS/Concepts`. Accessed: March 24 2023.

[79] Radu Bogdan Rusu and Steve Cousins. 3D is here: Point Cloud Library (PCL). In *IEEE International Conference on Robotics and Automation (ICRA)*, Shanghai, China, May 9-13 2011. IEEE.

[80] Point Cloud Library. `https://pointclouds.org/`. Accessed: March 27 2023.

[81] Martin Okrusch and Hartwig E. Frimmel. *Mineralogie.* Springer Berlin Heidelberg, 2022.

[82] M. Gmöhling, S. Köhl, J. Zevering, D. Borrmann, S. Ferrari, L. Penasa, R. Pozzobon, and A. Nüchter. Non-invasive identification of lunar rocks with optical and lidar systems. In *Proceedings of the 4th International Planetary Caves Conference* [83]. Abstract Nr. 1038.

[83] *Proceedings of the 4th International Planetary Caves Conference*, Haria, Spain, May 4-7 2023. `https://www.hou.usra.edu/meetings/4thcaves2023/authorindex/`. Accessed: June 14 2023.

Appendix

A Samples

(a)

(b)

(c)

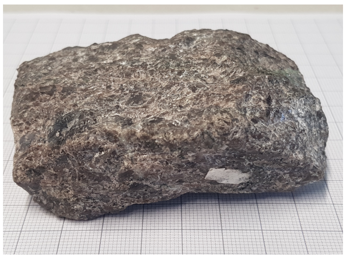

(d)

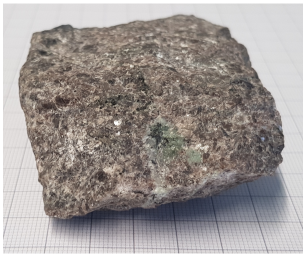

(e)

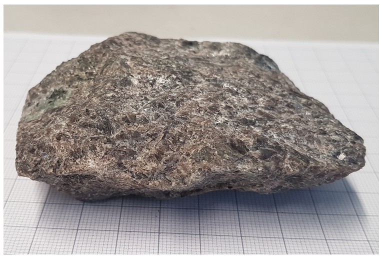

(f)

(g)

Figure 1: Anorthosite sample one (A1) without ice from multiple sides

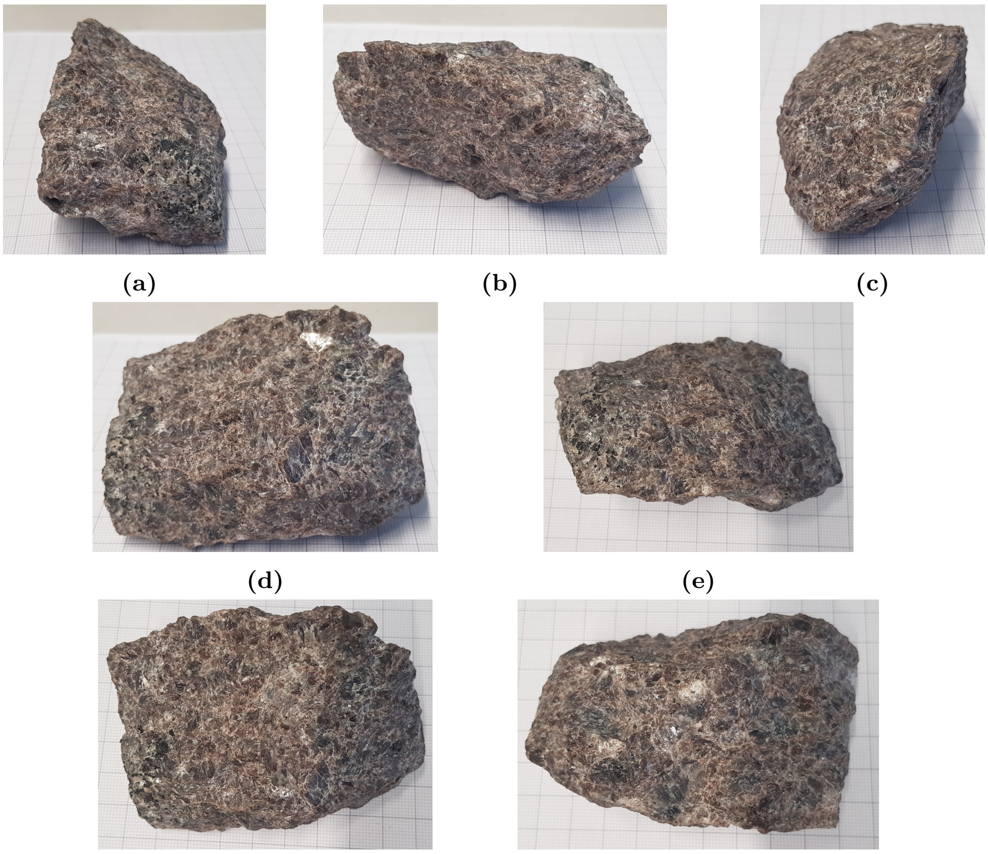

(a) (b) (c) (d) (e) (f) (g)

Figure 2: Anorthosite sample two (A2) from multiple sides

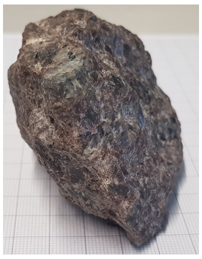

(a)

(b)

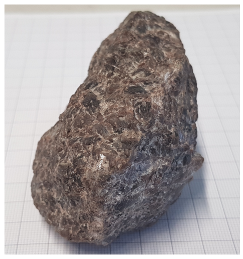

(c)

(d)

(e)

(f)

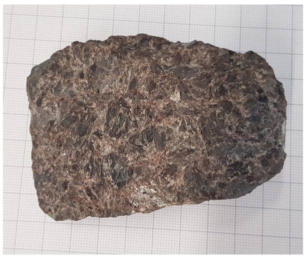

(g)

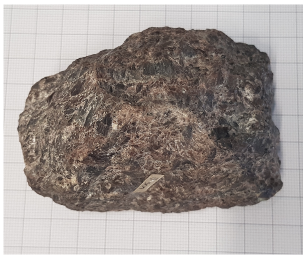

(h)

Figure 3: Anorthosite sample three (A3) from multiple sides

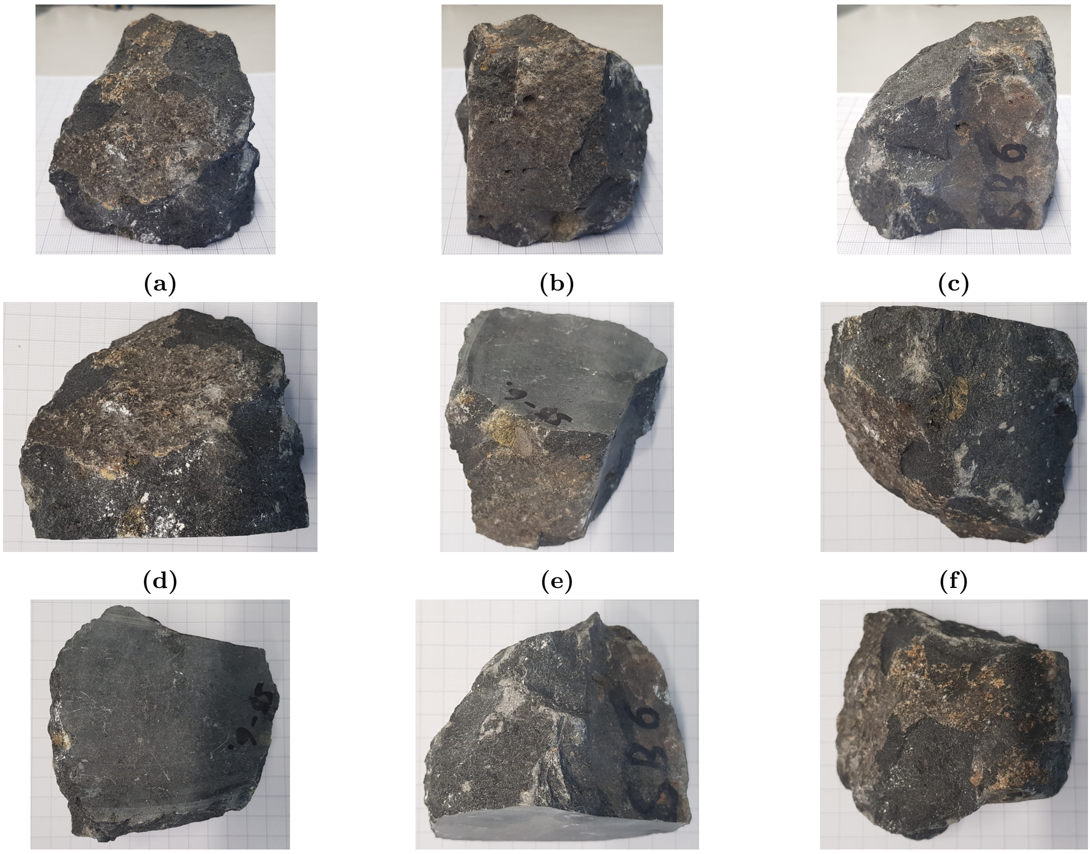

(a) (b) (c)

(d) (e) (f)

(g) (h) (i)

Figure 4: Basalt sample one (B1) without ice from multiple sides. Brown areas are due to weathering.

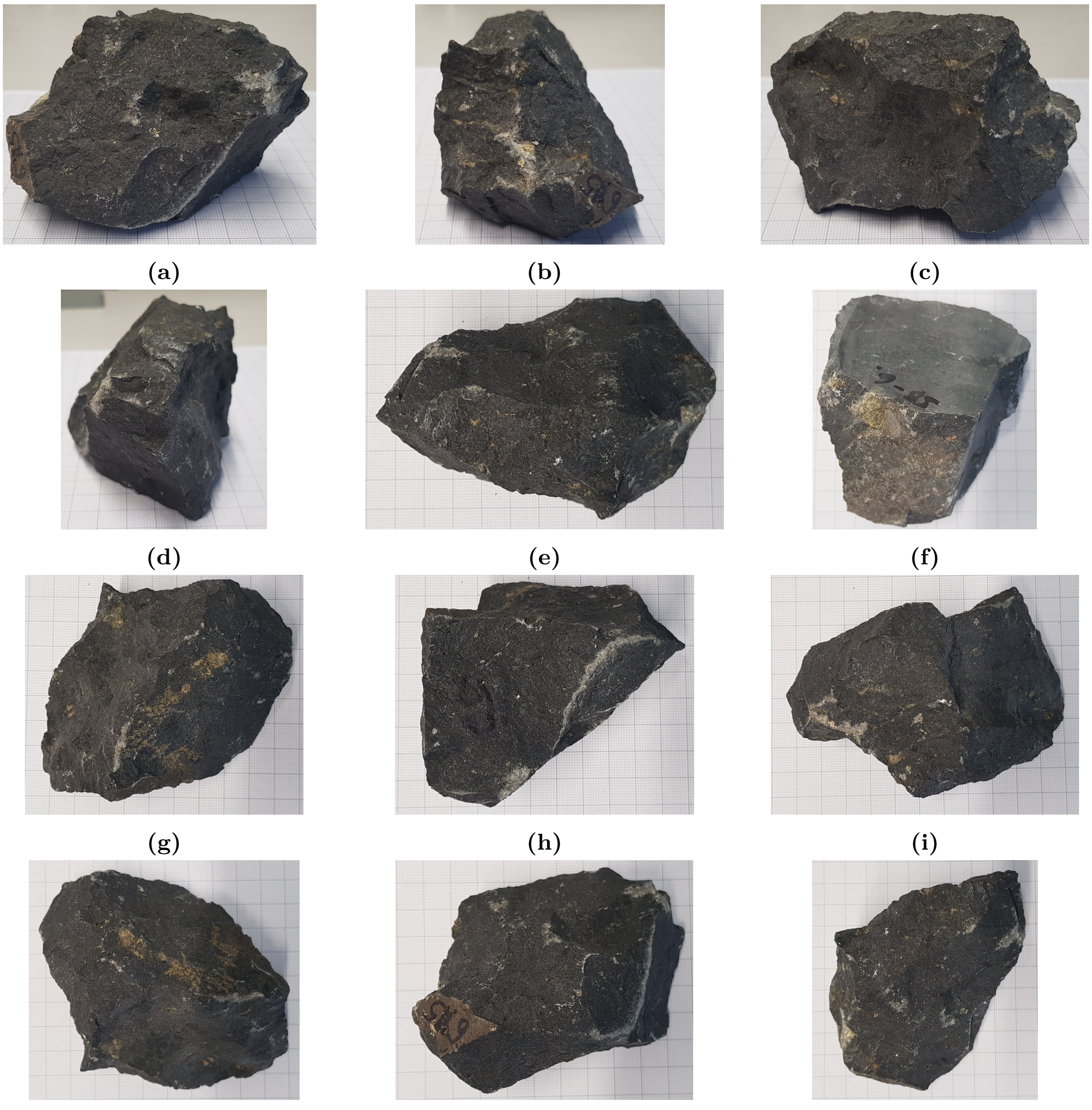

(a) (b) (c) (d) (e) (f) (g) (h) (i) (j) (k) (l)

Figure 5: Basalt sample two (B2) from multiple sides. Brown areas are due to weathering.

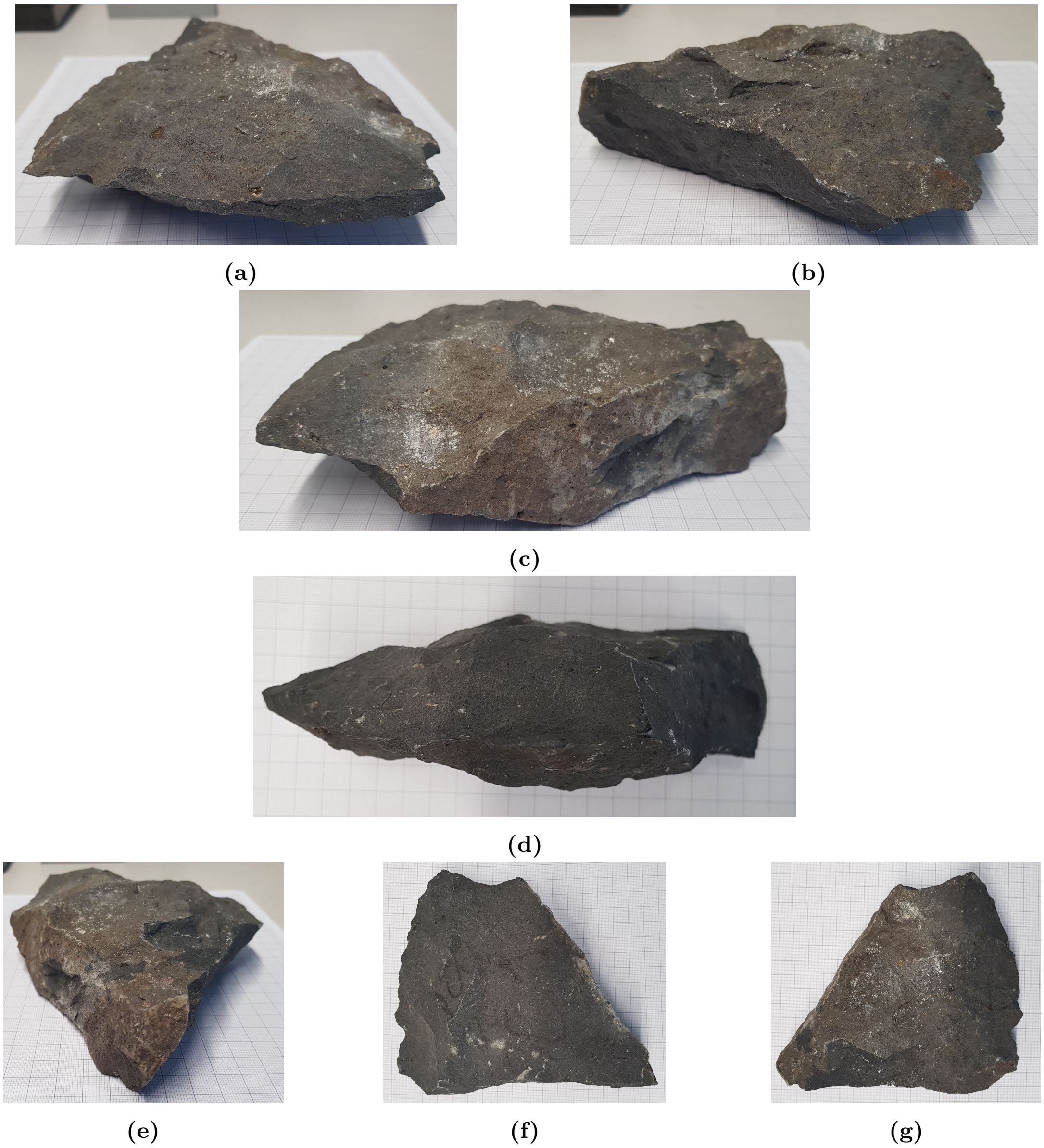

Figure 6: Basalt sample three (B3) from multiple sides. Brown areas are due to weathering.

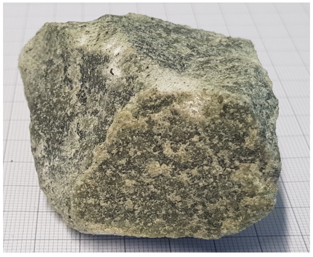

(a)

(b)

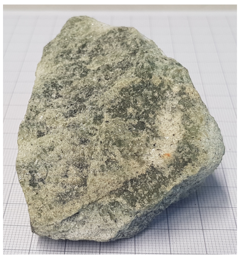

(c)

(d)

(e)

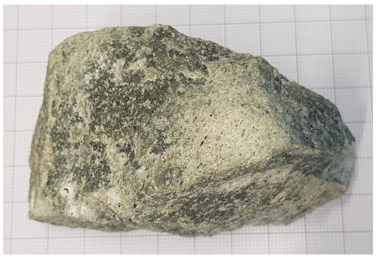

(f)

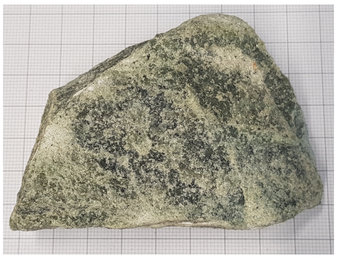

(g)

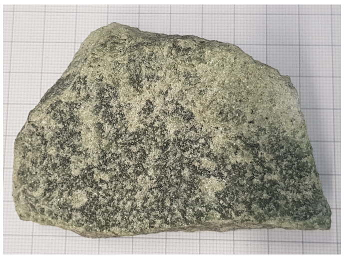

(h)

Figure 7: Dunite sample one (D1) without ice from multiple sides

(a)

(b)

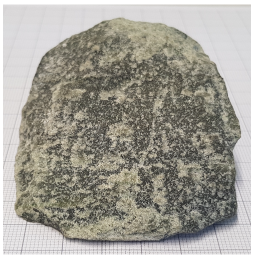

(c)

(d)

(e)

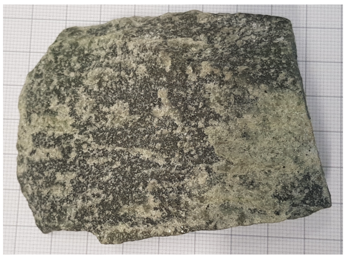

(f)

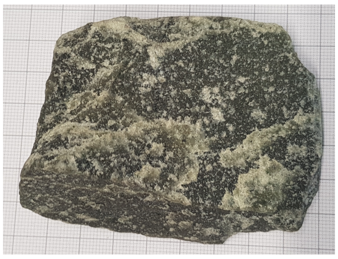

(g)

Figure 8: Dunite sample two (D2) from multiple sides

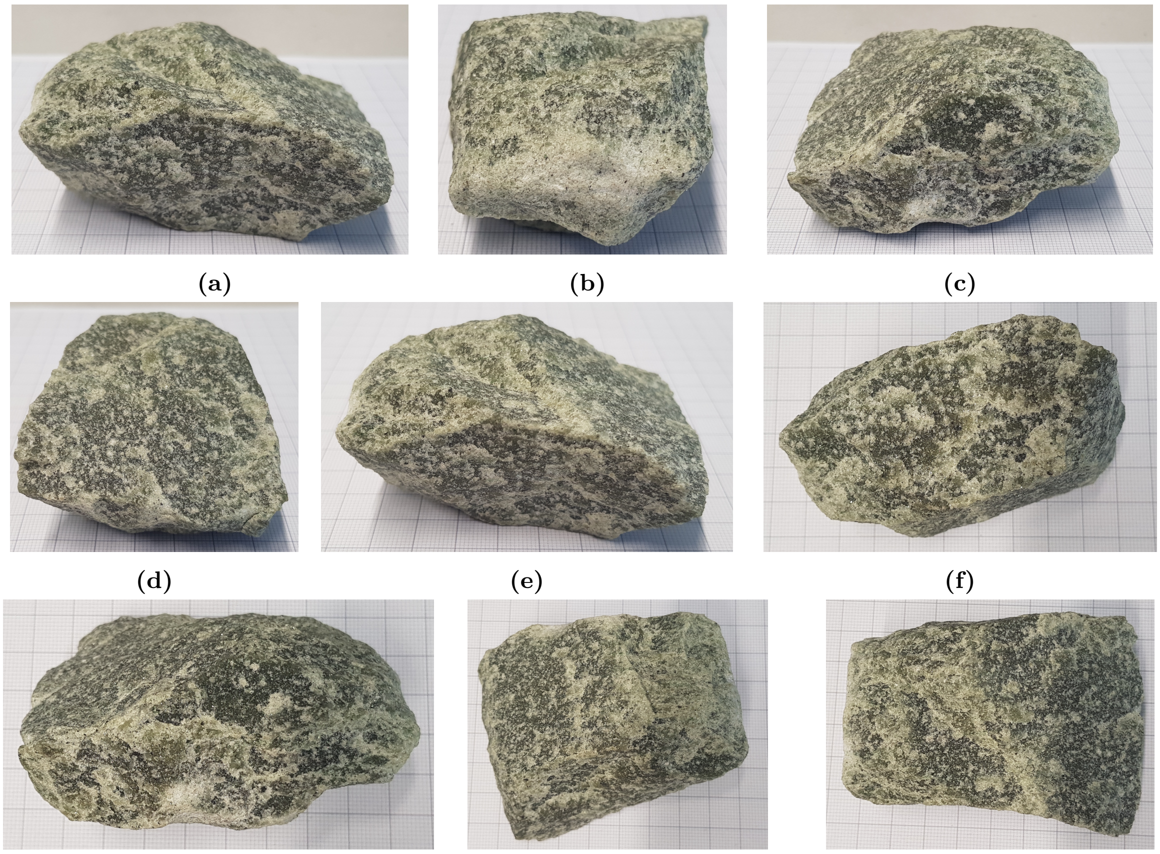

(a) (b) (c)

(d) (e) (f)

(g) (h) (i)

Figure 9: Dunite sample three (D3) from multiple sides

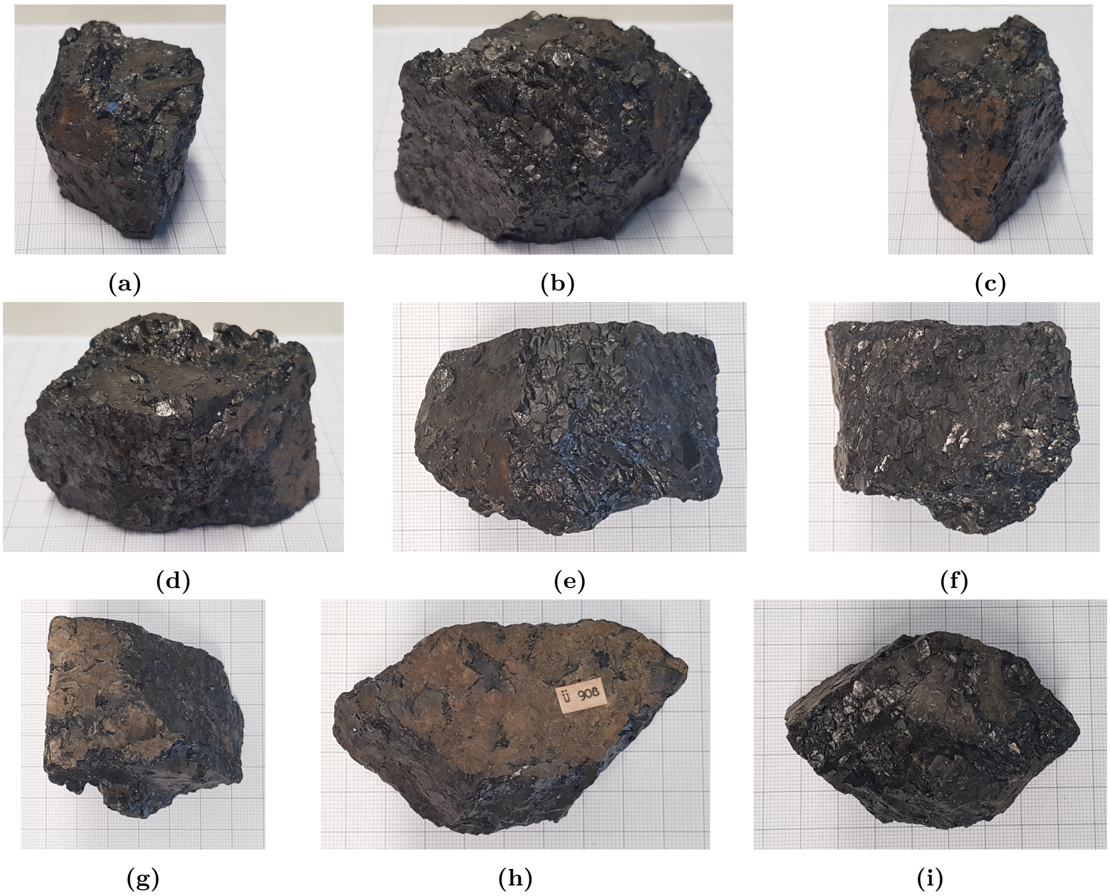

Figure 10: Ilmenite sample one (I1) without ice from multiple sides. Brown areas are due to weathering.

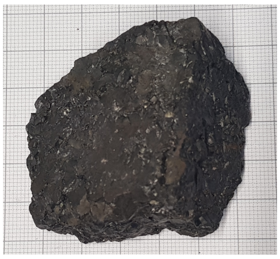

(a)

(b)

(c)

(d)

(e)

(f)

(g)

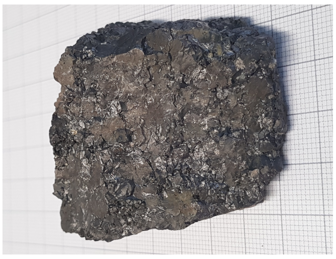

(h)

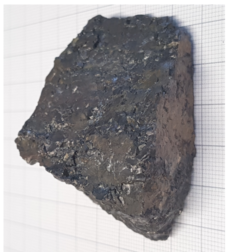

(i)

Figure 11: Ilmenite sample two (I2) from multiple sides. Brown areas are due to weathering.

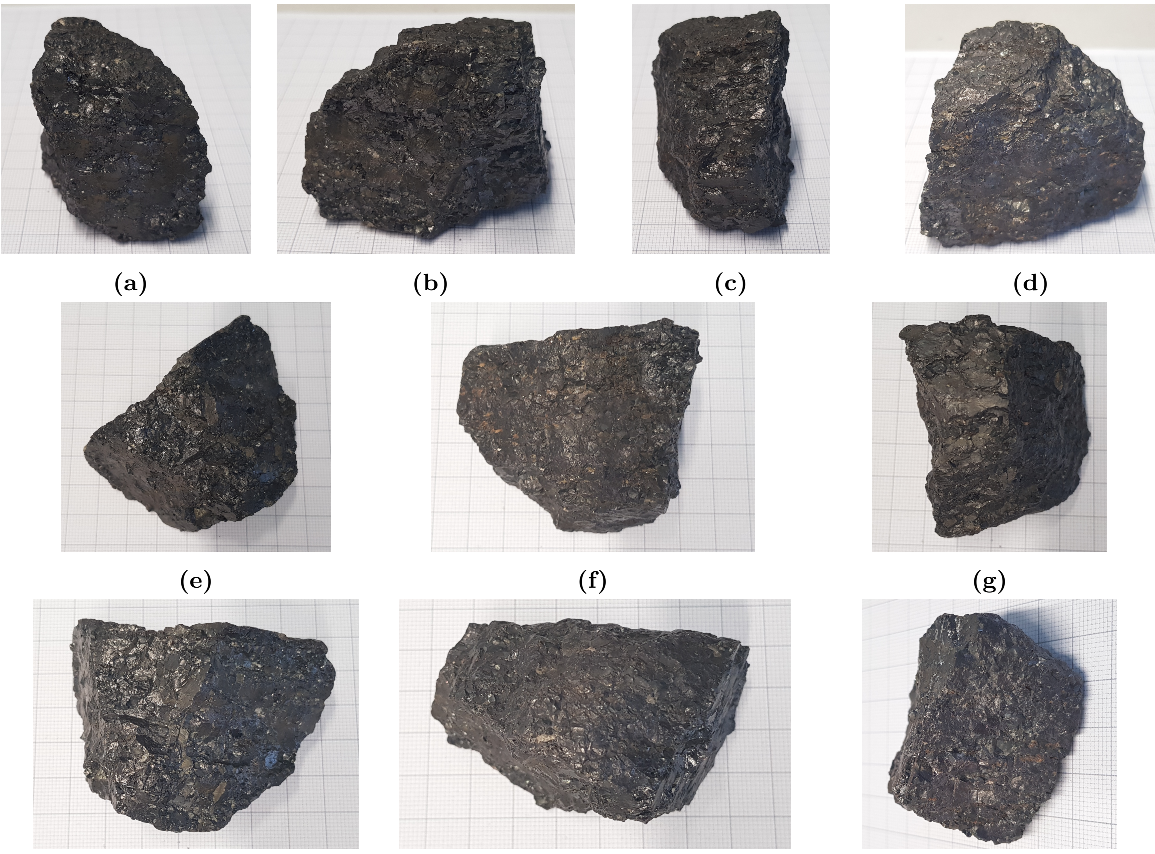

(a) (b) (c) (d) (e) (f) (g) (h) (i) (j)

Figure 12: Ilmenite sample three (I3) from multiple sides. Brown areas are due to weathering.

B Code

We provide the main code for extracting and normalizing intensity via `https://gitlab2.informatik.uni-wuerzburg.de/s391055/rock_analysis`. This excludes the code written for the RIEGL driver found in this Appendix.

Listing 1: Parameters file for the RIEGL ROS driver

```
riegl/ip: "192.168.1.125"

riegl/fov/min_line: 85.0
riegl/fov/max_line: 95.0
riegl/fov/min_frame: 0.0
riegl/fov/max_frame: 6.0
riegl/resolution/frame: 0.01
riegl/resolution/line: 0.01
riegl/mode: 1

log/interval: 0.01
log/timestamp: "timestamps.txt"
log/bagfile: "log.bag"
log/rxpfile: "raw.rxp"
log/basedir: "/home/sofie/logdata/"
log/scandir: "scan3d/"
```

Listing 2: Launch file for the RIEGL ROS driver

```
<launch>
  <!-- Load the configuration file -->
  <rosparam command="load" file="$(find␣riegl)/launch/parameters_rocks.yaml" />

  <node pkg="tf" type="static_transform_publisher" name="rieglcali" args="0␣0␣0
     ␣0␣0␣0␣odom_frame␣riegl␣100"/>
  <node pkg="riegl" name="rieglctr" type="ctr" respawn="true"/>

  <!-- Logging for assembling/calibrating scans afterwards -->
  <node pkg="riegl" name="rxploggersingle" type="rxploggersingle" />
  <node pkg="rclock" type="timepublisher" name="timepublisher"/>
  <node pkg="riegl" name="tslogger" type="tslogger" />
  <node pkg="bag2scans" name="record" type="record" />
  <node pkg="riegl" name="receiverESA" type="receiverESA" />

  <!--client that requests a full send and starts scan from riegl-->
  <node pkg="riegl" name="rockClient" type="rockClient" output="screen"/>
</launch>
```

Listing 3: ROS node calling services to start RIEGL scan and publication of the point cloud, located in the RIEGL ROS driver.

```
#include <ros/ros.h>
#include "riegl/Command.h"
#include "std_srvs/Empty.h"
#include "riegl/scanparams.h"

int main(int argc, char *argv[])
{
    ros::init(argc, argv, "rockClient");
    ros::NodeHandle client_handle;

    ROS_INFO("[rockClient]␣Starting␣client...");

    ros::ServiceClient sendFullClient = client_handle.serviceClient<std_srvs::
        Empty>("/sendFull");
    ros::ServiceClient SendingClient = client_handle.serviceClient<std_srvs::
        Empty>("/startSending");
    ros::ServiceClient MeasureClient = client_handle.serviceClient<std_srvs::
        Empty>("/startMeasuring");

    std_srvs::Empty srv;
    sendFullClient.waitForExistence();


    if(sendFullClient.call(srv) && SendingClient.call(srv) && MeasureClient.
        call(srv)){
        ROS_INFO("[rockClient]␣successfully␣requested␣scan␣from␣riegl");
    } else {
        ROS_ERROR("[rockClient]␣failed␣to␣call␣services␣for␣riegl");
    }

    return 1;

}
```

Proclamation

Hereby I confirm that I wrote this thesis independently and that I have not made use of any other resources or means than those indicated.

Würzburg, June 2023